AIAA JOURNAL
Vol. 45, No. 3, March 2007

Study of a Confined Turbulent Jet: Influence of Combustion and Pressure

C. Duwig* and L. Fuchs
Lund University, 221 00 Lund, Sweden
and
P. Griebel,† P. Siewert,† and E. Boschek†
Paul Scherrer Institut, 5232 Villigen PSI, Switzerland

DOI: 10.2514/1.26352

Today, environmental issues play an important role in the viability of modern low-emission power plants. As a consequence, gas turbine combustors need to be operated at lean premixed conditions. However, successful designs require a detailed knowledge of the combustion process under realistic operating conditions. The present study focuses on nonreacting and reacting jets at operating pressures from 1 to 14 bar. First, an isothermal confined jet has been studied experimentally and numerically using particle image velocimetry and large eddy simulation. The flow is highly turbulent and includes large-scale unsteady structures. The comparison of the numerical results and the experimental velocity data showed an excellent agreement that was generally below the numerical or experimental uncertainty. Second, the influences of combustion and operating pressure on the flowfield were investigated. The large eddy simulation results showed that the jet core was lengthened, due to the density jump across the flame. The effect of pressure on the flame was studied using planar laser-induced fluorescence and large eddy simulation at a constant Mach number. The flame brush and the velocity fields were found to be relatively insensitive to an increase of pressure from 1 to 14 bar (and, correspondingly, to an increase of Reynolds and Karlovitz numbers). The numerical results suggest that increasing pressure decreases the laminar flame speed and increases the flame-front wrinkling, causing the turbulent flame speed to be less sensitive to pressure.

Nomenclature

A	=	amplitude of the velocity spectrum
a	=	ratio between the filter length and the laminar flame thickness
c	=	progress variable based on a physical variable X: $c = (X - X_u)/(X_b - X_u)$
D	=	diffusivity or fractal dimension
D_L	=	diameter of the liner
Dp	=	diameter of the pipe at the combustor inlet
L_T	=	integral length scale
M	=	Mach number
P	=	operating pressure
R_{UV}	=	axial/radial component of the Reynolds stress tensor
r	=	signed radial coordinate
S_L	=	laminar flame speed with respect to the fresh gases
S_T	=	turbulent flame speed
St	=	Strouhal number, $f \cdot Dp/U_{\mathrm{BULK}}$
T	=	temperature, K
U_{BULK}	=	bulk velocity at the inlet, a constant in the present paper, 40 m/s
u_Δ	=	subgrid-scale velocity fluctuation
u'	=	turbulence intensity
X	=	axial coordinate
X_b	=	variable X in the burned gases
X_u	=	variable X in the fresh gases
Y_F	=	fuel mass fraction
Δ	=	filter length
Ξ	=	subgrid-scale wrinkling factor
ρ	=	density
Φ	=	fuel/air equivalence ratio
ω	=	reaction term
$\langle . \rangle$	=	time-averaging operator

Presented as Paper 0553 at the 44th AIAA Aerospace Sciences Meeting and Exhibit, Reno, NV, 9–12 January 2006; received 6 July 2006; revision received 29 November 2006; accepted for publication 8 December 2006.

*Faculty of Engineering (LTH), Division of Fluid Mechanics, Department of Energy Sciences, Box 118; Christophe.Duwig@vok.lth.se (Corresponding Author).

†Combustion Research.

I. Introduction

DUE to stricter emission regulations, environmental issues of power generation play an important role in the viability of modern power plants. To reduce harmful emissions, the current trend is to design premixed gas turbine combustors to operate at extremely fuel-lean conditions. Consequently, the peak temperature and NO_x emissions are reduced, but combustion instabilities leading to flash back, flame blowout, and high CO/UHC emissions may occur [1]. The challenge, therefore, is to understand and predict the unsteady combustion process under realistic conditions (i.e., at high pressure) and to design highly efficient, safe, low-emission combustors.

Turbulent combustion is very complex, because a wide range of physical and chemical scales are involved. Simulation of turbulent combustion is particularly difficult, because the phenomena involved are highly nonlinear and unsteady. In addition, a direct numerical simulation (DNS) of the problem is beyond current computing capability. However, current computational power enables the use of large eddy simulation (LES) tools for directly resolving large-scale flame fluctuations and capturing possible large-scale instabilities.

In the present paper, numerical and experimental studies of a confined jet and jet flame were performed. Turbulent free jets have been numerically studied using LES for about one decade (e.g., [2–6]), whereas experimental investigations have been performed for a much longer time. In the jet core, close to the nozzle exit, the axial velocity along the jet axis remains constant. Farther downstream, the axial velocity starts to decrease, which corresponds to the end of the jet core. At moderate Reynolds numbers, LES studies showed that the influence of vortex rings results from a Kelvin–Helmholtz type of instability. These vortices are formed in the shear layer around the jet core and are convected downstream until they merge. These vortex

rings contribute to the mass and momentum exchange between the jet and the surroundings. Because vortex pairing is an efficient way of momentum exchange, an increase in momentum transfer is visible after pairing. DaSilva and Métais [6] showed that the inflow conditions can trigger vortex pairing. Consequently, one can shorten the jet core by adjusting the mean flow and turbulence properties upstream of the jet orifice.

An experimental investigation of a confined jet was performed by Dellenback et al. [7]. They studied the turbulence characteristics of a sudden expansion, confined jet flow with and without swirl and found no effect of the Reynolds number on the flowfield. Kobayashi et al. [8] measured turbulence intensities and integral length scales in a turbulent free jet and found a weak pressure dependence (i.e., almost no effect of the Reynolds number). As a result of these observations, it has become a common practice to perform pressure-variation experiments at a constant inlet jet velocity. In this way, the Reynolds number increases linearly with pressure, but the integral length scale and turbulence intensity remain almost constant.

Because of their fundamental and practical relevance and their relative simplicity, turbulent jet flames (Bunsen-type flames) have received considerable attention in literature. Turbulent jet flames are simpler to model than swirling flames, but are themselves rather complex systems. In addition to the physical phenomena described earlier, the thermal expansion due to combustion has to be taken into account. Laboratory experiments related to premixed, free jet flames using laser techniques are quite common. However, detailed measurements of both velocity and flame properties are much less common. Detailed investigations of the structure of methane/air flames stabilized on a turbulent Bunsen-type burner were performed by Chen et al. [9] and Buschmann et al. [10]. These flames fall mainly into the *wrinkled-flamelets* or *corrugated-flamelets* regimes. Chen et al. measured the velocity and the species concentrations in a piloted, stoichiometric Bunsen-type flame at ambient temperature and pressure. They observed that the thermal expansion decreases the momentum transfer between the core and the surrounding and therefore lengthens the jet core. The effects of pressure on the propagation and structure of methane/air flames were investigated by Kobayashi et al. [11] and Lachaux et al. [12]. Some of these flames belonged to the *thickened-flames* (*thin-reaction-zones*) regime (Karlovitz number $Ka > 1$), but the operating conditions in these experiments were still not completely relevant for gas turbines. Lachaux et al. stated that an increase in pressure leads to higher flame-front wrinkling. For methane/air flames, which are characterized by a strong inverse dependence of the laminar flame speed on pressure ($S_L \sim P^{-0.5}$, given by Kobayashi et al.), this enhanced flame-front wrinkling is considered to be one of the compensation mechanisms leading to a weak or nonexistent pressure dependence of the turbulent flame speed S_T. However, more detailed investigations are necessary to clarify the net effect of pressure on turbulent flame speed. An experimental study at operating conditions relevant to gas turbines was performed by Griebel et al. [13–15]. They investigated preheated lean premixed jet flames at pressures up to 15 bar. No influence of pressure on the flame-front position, flame-brush thickness, or turbulent flame speed was found.

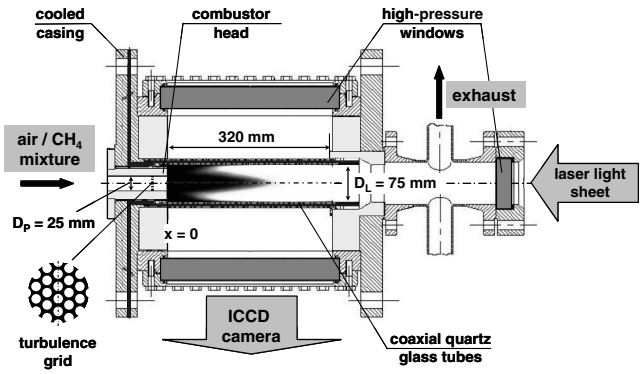

Fig. 1 High-pressure combustion chamber.

The present paper uses the geometry studied by Griebel et al. [13–15] to investigate in detail the influences of combustion and pressure on a confined jet flame. In the following section, the combustion chamber and experimental techniques are described. In the third section, the LES combustion model used in the simulations is presented. The fourth section describes the operating conditions of this investigation. The results and the accuracy of the LES tool are discussed in the fifth section, using a comparison with experimental results and sensitivity analysis. It also includes a comparison between different operating conditions. Finally, conclusions are drawn regarding the flame dynamics and the influences of combustion and pressure on the jet turbulence.

II. Experimental Setup and Measuring Techniques

A. Experimental Facility and Boundary Conditions

The combustion experiments were carried out in a generic high-pressure combustor [13–16], shown in Fig. 1. The combustor is capable of operation at a pressure of up to 30 bar, with a maximum airflow rate of 750 m_N^3/h (0.3 kg/s) and exhaust gas temperatures up to 1850 K. The combustor has a maximum thermal power of 400 kW and the combustion air can be electrically preheated as high as 823 K. The combustion air and the fuel are fully premixed through static mixers. The cylindrical liner is composed of two convectively air-cooled coaxial quartz glass tubes (inner quartz glass tube diameter $D_L = 75 \times 10^{-3}$ m).

The sources of total combustor heat losses are the air cooling, the water cooling of the casing (conductive and convective heat loss), and the radiation heat loss through the windows. A comparison of the measured exhaust gas temperatures, adiabatic flame temperatures, and calculated exhaust gas temperatures, including the effects of combustor heat losses (air and water cooling), showed that the heat loss due to radiation is negligible in the present case [16]. Therefore, the total heat loss of the combustor can be estimated by measuring the air and water mass flows and the inlet and outlet temperatures of the cooling air and the cooling water. The relative heat loss is the highest at atmospheric pressures ($\sim$11% of total thermal load) and decreases with pressure down to $\sim$4% at 14 bar. At 5 bar, the relative heat loss is $\sim$6% of the total thermal load; thus, above 5 bar, the combustor can be treated as almost adiabatic [16].

The flame is stabilized aerodynamically by the recirculation of hot combustion gases induced by the geometry with sudden expansion. The combustor has an inlet diameter of $Dp = 25 \times 10^{-3}$ m and is equipped with high-pressure windows to provide optical access to the entire length of the combustor. A turbulence grid with hexagonally spaced holes is placed in the inlet channel to control the turbulence quantities u' and L_T of the jet. The grid used in the present investigation is characterized by a blockage ratio of 50% and a grid-hole diameter of 3×10^{-3} m. The grid is placed 30×10^{-3} m upstream of the combustor inlet ($X/Dp = 0$). This distance corresponds to 10 grid-hole diameters and it was chosen to assure a homogeneous distribution of the turbulence characteristics u' and L_T at the combustor inlet in the radial direction.

At the combustor inlet, u' and L_T are roughly constant along the radius; however, toward the burner lip, it was not possible to accurately measure the velocity statistics, due to high laser light reflections. Details about the velocity fluctuations will be described in Sec. V. At the combustor inlet, the integral length scale $L_{T,xx}$ (based on the axial velocity component u in the axial direction x) calculated from PIV data equals $\sim$2.5 mm. The values of $L_{T,xx}$ at this location are mainly influenced by the grid-hole diameter and the dissipation of small scales within the inlet channel. It is worth mentioning that the accuracy of the L_T measurement is limited by the spatial resolution of the PIV measurements (discussed in the following section). At the combustor exit ($\approx$12 Dp), the radial profile of the integral length scale is flat. The values are roughly equal ($L_{T,xx} \approx 11$ mm) and are mainly controlled by the geometry of the combustor [16].

Flame characteristics were studied in the high-pressure combustor using planar laser-induced fluorescence of the OH radical (OH-

PLIF). A detailed experimental database is available for the present jet flame [14,15].

The turbulent flowfield quantities of the present paper were measured with particle image velocimetry (PIV) in a model combustor. This combustor is operated at atmospheric pressure and is geometrically identical with the high-pressure combustor (Fig. 1), but has a much simpler design. This simplified test apparatus was used for two reasons. First, the model combustor allowed for efficient suppression of laser light reflections explicitly in the region close to the combustor head (metal surface). Second, a relatively easy cleaning of the seeding depositions on the quartz glass tube walls was possible. The turbulence grid was located 0.19 m (7.6 Dp) downstream of the static mixer and 30×10^{-3} m (1.2 Dp) upstream of the combustor inlet. The geometric and aerodynamic similarity of the model and the high-pressure combustor chamber was verified before the actual measurements. The flowfield results (e.g., turbulence intensity u') measured in both combustors show only minor differences, well below the measuring accuracy.

B. Measuring Techniques

1. *Particle Image Velocimetry*

The turbulent flowfield was characterized using two-dimensional particle image velocimetry (2-D PIV). These measurements were performed in the model combustor at atmospheric and isothermal conditions (without combustion). The entire flowfield of the combustor was captured in four overlapping camera positions using a 12-bit CCD camera (Image Intense from LaVision) with a chip resolution of 1040×1376 pixels. The Nikkon lens ($fo = 35 \times 10^{-3}$ m) was equipped with a narrow bandpass filter (532 nm). This arrangement results in a spatial resolution of approximately 80 μm/pixel. The flow was seeded with oil droplets generated in a Laskin nozzle seeder. The average size of the oil droplets measured with phase Doppler anemometry (PDA) was approximately 2 μm. Such a small seeding droplet size assures a sufficiently high-frequency response [17]. The green (532-nm) laser light emitted by a Twin-Nd/YAG laser (Quantel) was formed into a parallel light sheet by a set of lenses (two spherical lenses and one cylindrical). The height of the light sheet that illuminated the oil particles was equal to the inner diameter of the quartz glass liner ($D_L = 75 \times 10^{-3}$ m), and its average thickness was estimated to be less than 1×10^{-3} m. The position of the light sheet waist was adjusted using a spherical lens ($fo = 1500 \times 10^{-3}$ m) to be approximately in the middle of the combustor chamber length ($x \approx 160 \times 10^{-3}$ m). The PIV images were postprocessed using a commercial software (DaVis) based on cross-correlations with an adaptive window algorithm [18]. The final window size was 16×16 pixels, with 50% window overlapping, resulting in a final spatial resolution of the vector field of $\approx 0.64 \times 10^{-3}$ m. The estimated dynamic range of the velocity measurements with PIV was $\approx$80. For every camera position, 400 instantaneous images were measured and postprocessed. This number of samples is a trade-off between accuracy of the turbulence statistics, measuring time, and the computational time for postprocessing. Using 400 samples results in an estimated uncertainty of the root mean square (RMS) of the velocity fluctuations (u_{RMS} and v_{RMS}) of about 7% of the measured variable (assuming that the velocity sample distributions are of a Gaussian type).

2. *Planar Laser-Induced Fluorescence*

The flame-front characterization was based on the measurements and postprocessing of single-shot, planar laser-induced fluorescence images of the OH radical. The OH-PLIF measurements were performed using laser light emitted by a Nd/YAG/dye laser system (Quantel), and the OH-PLIF images were recorded with a 12-bit ICCD camera (PCO, DiCamPro). The camera was mounted perpendicular to the axis of symmetry of the combustor, at a distance sufficient to capture the full combustor length. The camera chip had a resolution of 1280×1024 pixels. An achromatic lens system ($fo = 100$ mm, Halle) was equipped with a set of bandpass filters (BK 310-11-C, centered at 310 nm), allowing for a high light transmission in the UV range of OH fluorescence. The laser light was formed into a parallel light sheet by a set of lenses centered in the measuring section through the axial high-pressure window (see Fig. 1). The excitation wavelength used in the OH-PLIF measurements was 285 nm.

The calculation of the mean progress variable is based on the postprocessing and statistical analysis of the single-shot OH-PLIF images. The postprocessing algorithm is based on the detection of the OH signal intensity gradient in the reaction zone. The sequence of image processing operations is described next. As a first step, the images are binned (2×2) from the recording resolution of 1260×300 pixels into 630×150 pixels that correspond to a decrease of the spatial resolution from 0.25×10^{-3} m/pixel to 0.5×10^{-3} m/pixel. This is done to increase the signal-to-noise ratio and reduce the postprocessing time (which depends on the image size). Additionally, an iterative median filter (5×5 pixels) was applied to suppress image noise. Next, the threshold operation was applied to every single-shot OH-PLIF image, to calculate a binary representation of the instantaneous progress variable. A constant threshold of 25% of the maximum signal intensity of the corresponding average OH-PLIF image was used. This threshold value was found to qualitatively provide the best results in terms of flame-front detection. A similar threshold value was also used in the work of Deschamps et al. [19]. The sensitivity of the progress variable results to the chosen threshold value was investigated by changing the threshold value in the range of 15 to 30%. This did not change the flame-brush thickness, defined as the distance between the leading edge of the flame front ($\langle c \rangle = 0.1$) and the surface for which $\langle c \rangle = 0.5$. Increasing the threshold changed the flame-front position at the centerline (defined by the axial location of the progress variable value $\langle c \rangle = 0.5$) by $\approx$10%.

Assuming an infinitely thin flame front (infinitely fast chemistry approach), the progress variable is a step function separating unburned mixture and burned gas. This approach is used in the experimental data, in which the OH-PLIF intensity values above the threshold are assigned to a progress variable equal $c = 1$, which represents the combustion products (burned gas). The values lower than the threshold are assigned to $c = 0$, which represents the fresh gas (unburned) mixture. An averaging of 800 single shots yields a two-dimensional image representing the spatial distribution of the mean progress variable $\langle c \rangle = 0 \div 1$. A typical example is given in Fig. 1 [$\langle c \rangle = 0$ (black), $\langle c \rangle = 1$ (white)].

III. Numerical Procedure

A. Governing Equations and Subgrid-Scale Transport Modeling

In the present paper, a numerical investigation of a jet and jet flame is considered. In the LES framework, the filtered governing equations for reacting low Mach number flows are [20]

$$\frac{\partial \bar{\rho}}{\partial t} + \nabla(\bar{\rho}\tilde{\boldsymbol{u}}) = 0 \tag{1}$$

$$\frac{\partial \bar{\rho}\tilde{\boldsymbol{u}}}{\partial t} + \nabla(\bar{\rho}\tilde{\boldsymbol{u}}\tilde{\boldsymbol{u}}) = -\nabla\bar{P} + \nabla(-\overline{\rho\boldsymbol{u}\boldsymbol{u}} + \bar{\rho}\tilde{\boldsymbol{u}}\tilde{\boldsymbol{u}} + \mu\nabla\tilde{\boldsymbol{u}}) \tag{2}$$

$$\frac{\partial \bar{\rho}\tilde{Y}_i}{\partial t} + \nabla(\bar{\rho}\tilde{\boldsymbol{u}}\tilde{Y}_i) = \nabla(-\overline{\rho\boldsymbol{u}Y_i} + \bar{\rho}\tilde{\boldsymbol{u}}\tilde{Y}_i + \rho D_i \nabla\tilde{Y}_i) + \bar{\omega}_i \tag{3}$$

$$\frac{\partial \bar{\rho}\tilde{T}}{\partial t} + \nabla(\bar{\rho}\tilde{\boldsymbol{u}}\tilde{T}) = \nabla(-\overline{\rho\boldsymbol{u}T} + \bar{\rho}\tilde{\boldsymbol{u}}\tilde{T} + \rho D_T \nabla\tilde{T}) + \bar{\omega}_T \tag{4}$$

$$\bar{\rho} = \overline{\left(P/RT\right)} \tag{5}$$

where $\boldsymbol{u}$ is the velocity vector, μ is the viscosity, R is the specific ideal

gas constant, D_i is the diffusivity of species i, Y_i is the mass fraction of species i, and ω_i is the reaction rate of species i. The overbar denotes the spatial filtering operation and the tilde denotes the density-weighted spatial filtering, so that

$$\tilde{Q} = \overline{\rho Q}/\bar{\rho} \tag{6}$$

The spatial filtering corresponds to a low-pass filter that removes all Fourier components having shorter length scales than the filter size. The filtering operator is linear and is assumed to be commutative with time-and-space derivatives. The filtering operation is not commutative with nonlinear terms. Thus, nonlinear terms lead to expressions that cannot be expressed in terms of the filtered quantities. These terms are gathered on the right-hand side (RHS) in the preceding equations and are called subgrid-scale (SGS) terms. Expressing these SGS terms in terms of filtered quantities is required for closing the system. The main role of the SGS terms is to account for the interaction between the resolved and the unresolved scales. In the momentum equations, the SGS terms should account for the dissipative character of turbulence on the small (unresolved) scales as well as for the transfer of energy among the resolved and unresolved scales. Similar SGS properties may be attributed to the SGS in the temperature and the species-transport equations.

A computational grid can support only Fourier components that have longer wavelengths than the grid size. Thus, a dependent variable represented on a grid used together with a discrete approximation for the derivatives leads to an *implicit* filtering. If no explicit SGS terms are added, then the numerical scheme should at least account for the small-scale dissipation. This is attained for any numerically stable scheme [21,22]. However, overly dissipative numerical schemes are highly inappropriate for LES, because in addition to dissipation on small scales, they may be also too dissipative on the larger scales. This effect can be avoided by choosing appropriate (higher-order) discretizations. In addition, the spatial resolution has to be fine enough, virtually on the order of magnitude of the Taylor microscale. With such a resolution, the energy transfer among the scales is dissipation-independent and therefore the numerical scheme may act implicitly as an SGS model. However, one should keep in mind that this implicit SGS approach may require a better resolution than a corresponding LES that uses advanced SGS models. Nevertheless, even with an explicit SGS model (such as the dynamic model), the spatial resolution has to be adequate [21,22]. In the present paper, we use a third-order upwind scheme [23]. Consequently, the leading term of the truncation error corresponds to a hyperviscosity that acts as an *implicit* SGS model. Using the same scheme, Revstedt et al. [24] showed that traditional SGS models do not perform significantly better than the implicit approach for simulations of a turbulent jet. Therefore, the implicit approach is used in this paper for closing the filtered momentum transport equations.

B. Overview of Combustion Modeling

If LES is a suitable technique for resolving large structure dynamics and flow instabilities in combustors, no ultimate solution has been yet proposed to model the filtered reaction rates. Early results using LES for capturing combustion instabilities are promising [18]. However, issues such as the influence of the subgrid-scale modeling on the flame dynamics still need to be addressed.

So far, only a few LES combustion models have been proposed. One might cite implicit LES (ILES) techniques [25] that solve monotonically integrated equations (1–4) and do not require any explicit model. Among the explicit models, one can distinguish between two categories, depending on how the density change across the thin flame front is treated. It has been proposed to artificially thicken the flame front to resolve it directly on the LES grid, while ensuring that the flame propagation speed is kept constant [18,26]. This thickening makes the technique numerically stable, but at the cost of changing the flame dynamics and the flame response (e.g., in case of a curved flame front). Another possibility is to approximate a flame structure and average/filter it to get the combustion SGS contribution. Several ways have been proposed: 1) assuming an infinitely thin flame front propagating at the SGS flame speed (G equation) [27]; 2) solving the filtered propagative form of the c equation, assuming an infinitely thin flame front [28–30]; 3) assuming a laminar structure and reconstructing the subgrid-scale effects using the LES spatial filtering properties [30,31]; 4) assuming the flame structure via a beta PDF [32]; and 5) solving a 1-D equation for the flame front using Arrhenius chemistry and modeled stochastic mixing [linear eddy model (LEM)] [33]

It is worth noting that the choice of a beta-PDF shape is a purely numerical approximation. LEM is very CPU-expensive and highly dependent on the mixing model used to "stir" the 1-D flame front. The G equation (so-called Hamilton–Jacoby equation) is known to introduce additional numerical problems. Flamelet models based on the c equation require capturing of steep gradients, because the flame is spread on few filter lengths. However, with the help of advanced numerical techniques [34], these types of models have proven to be suitable for large eddy simulation of premixed turbulent combustion [30,31].

C. Filtered Flamelet Model for Premixed Combustion

The set of equations describing the fuel oxidation contains the transport equations for the considered chemical species and for the enthalpy. The complete set of equations detailing the oxidation of natural gas is far too large to be used for numerical simulations, and a reduced formulation is needed. In the present approach, the flamelet assumption allows a simplified coupling of turbulence and chemistry [20,27]. The combustion process is described by a single parameter called the progress variable c, which is related to the advancement of the reaction and is, by definition, zero in the unburned mixture and one in the burned gases. We define c by normalizing the fuel mass fraction and rewrite Eq. (3) to be

$$\frac{\partial \bar{\rho}\,\tilde{c}}{\partial t} + \nabla(\bar{\rho}\,\tilde{\boldsymbol{u}}\,\tilde{c}) = \nabla(-\overline{\rho \boldsymbol{u} c} + \bar{\rho}\,\tilde{\boldsymbol{u}}\,\tilde{c}) + \nabla(\overline{\rho D_{\mathrm{th}} \nabla c}) + \bar{\omega}_c \tag{7}$$

The left-hand side of Eq. (7) contains the unsteady and convective terms. The right-hand side contains the diffusion, the reaction, and the subgrid-scale transport.

A major difficulty in LES of reacting flows is that chemical reactions occur at scales much smaller than the filter length and therefore are not resolved and require modeling. In addition, the sum of the three terms on the right-hand side of Eq. (7) should model the premixed flame propagation accurately. In the present paper, a premixed flamelet formulation proposed by Duwig and Fuchs [31] has been used to close the filtered c equation. This approach consists of modeling the three unclosed terms of Eq. (7) by a reactive-diffusive balance, ensuring correct flame propagation. The right-hand side of Eq. (7) is modeled by a diffusion term plus a production term π, as follows:

$$\frac{\partial \bar{\rho}\,\tilde{c}}{\partial t} + \nabla(\bar{\rho}\,\tilde{\boldsymbol{u}}\,\tilde{c}) = \rho_0 D_0 \nabla^2 \tilde{c} + \pi(\tilde{c}, D_0) \tag{8}$$

Note that π is defined to be the RHS of Eq. (7) minus the diffusion term. The π term contains information related to the nongradient subgrid transport as well as the creation (source) of c. Furthermore, the π term defined by Eq. (8) is distributed over one–two filter lengths. Assuming that the source of c (i.e., the reaction layer of the premixed flame) is thin compared with the grid size (valid in the flamelet and thin-reaction-zones regimes), Duwig and Fuchs [31] suggested to model π using a Gaussian distribution so that $\pi = \alpha/\Delta \cdot (6/\pi)^{0.5} \cdot \exp[-6 \cdot (x/\Delta)^2]$, where x is the distance to the reaction layer, α is the integral burning rate, and Δ is the LES filter length. The burning rate is related to the laminar flame speed and the subgrid flame wrinkling, so that $\alpha = \rho_u S_L \Xi$. Further, a nondimensional parameter $a = (\rho_u S_L \Xi \Delta)/\rho_0 D_0$ emerges in Eq. (8). Finally, a relation $x(c)$ is needed to close Eq. (8). In the limiting case of a quasi-planar flame, Duwig's and Fuchs's analysis provides an expression for the term $\pi\Delta/\alpha = \Pi(c, a)$ that is stored in lookup tables [31]. The closed c equation is

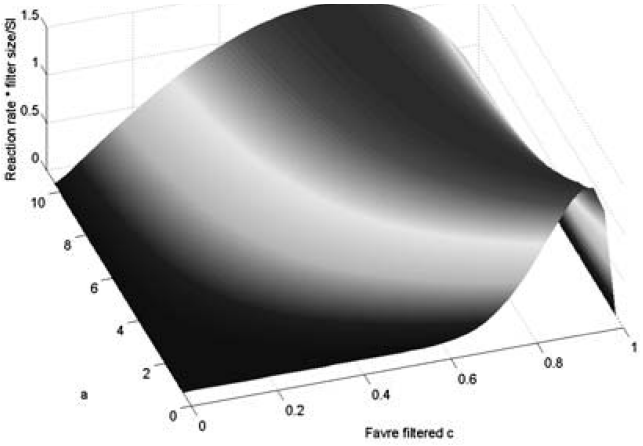

Fig. 2 Normalized production term Π_C in a Favre-filtered c/a space.

$$\frac{\partial \bar{\rho}\,\tilde{c}}{\partial t} + \nabla(\bar{\rho}\,\tilde{\boldsymbol{u}}\,\tilde{c}) = \frac{\rho_u S_L \Xi \Delta}{a}\nabla^2\tilde{c} + \rho_u S_L \Xi \frac{1}{\Delta}\Pi_c(\tilde{c}, a) \tag{9}$$

where Π_c is the production term and a is a nondimensional number comparing the filter size and the laminar flame thickness δ ($a = \Delta/\delta$). Figure 2 shows the production term mapped in a c/a space. For high a values, Π_c tends toward a parabolic shape, whereas for $a \sim 1$, its maximum shifts toward $c \sim 0.8$. For $a \sim 1$, the filter effect on the flame front is relatively low, so that Π_c approaches the laminar reaction rate.

D. Extension Toward Simulation of Thin Reaction Zones

The model previously presented is formally restricted to the so-called flamelet regime [20,27] (i.e., operating at $Ka < 1$). Peters's [27] analysis of the turbulence-combustion interaction shows that for a Karlovitz number above one, the smallest turbulent structures enter the preheating zone of the premixed flame. The small eddies modify the flame structure, but they are not small enough to penetrate the reaction zone. The flame front is broadened by turbulence, but the oxidation occurs in a small layer that is called the thin reaction zone [27]. The thin-reaction-zones regime is believed to cover the range of $1 < Ka < 100$ [27].

To extend the c-equation model, include the flame structure modification into Eq. (9). In the flamelet regime, the filtered flame structure depends on the laminar flame thickness δ and on the filter size and is characterized by the nondimensional number a. In the thin-reaction-zones regime, the flame-front thickness might be increased by turbulence. Therefore, a does not remain constant but becomes a function of the flow properties. We consider Eq. (9) and model the thickening (arising from the penetration of turbulent structures in the preheating zone) by an effective turbulent diffusion coefficient ρD_E, resulting in

$$\frac{\partial \bar{\rho}\,\tilde{c}}{\partial t} + \nabla(\bar{\rho}\,\tilde{\boldsymbol{u}}\,\tilde{c}) = \Xi(\rho_u S_L \delta + \rho D_E)\nabla^2\tilde{c} + \rho_u S_L \Xi \frac{1}{\Delta}\Pi_c \tag{10}$$

However, the effective diffusion needs to be closed. It corresponds to the effect of turbulent structures that are smaller than the preheating zone thickness l. Assuming a Kolmogorov energy cascade with constant transfer rate, one may relate ρD_E to the subgrid diffusivity ρD_Δ or to the subgrid velocity fluctuation u_Δ as

$$\rho D_E \approx \rho D_\Delta \left(\frac{1}{\Delta}\right)^{4/3} \approx \rho C l u_\Delta \left(\frac{1}{\Delta}\right)^{1/3} \tag{11}$$

where C is a model constant. Estimating $l \sim \delta/2$, one may rewrite Eq. (10) so that

$$\frac{\partial \bar{\rho}\,\tilde{c}}{\partial t} + \nabla(\bar{\rho}\,\tilde{\boldsymbol{u}}\,\tilde{c}) = \Xi\rho_u S_L \delta\left[1 + \frac{C u_\Delta}{2S_L}\left(\frac{\delta}{2\Delta}\right)^{1/3}\right]\nabla^2\tilde{c} + \rho_u S_L \Xi \frac{1}{\Delta}\Pi_c \tag{12}$$

One might define an effective number b that accounts for the thickening as

$$b = \frac{a}{1 + 2^{-4/3} C \frac{u_\Delta}{S_L}\frac{1}{a^{1/3}}} = \frac{a}{1 + 2^{-4/3} C K a_\Delta^{2/3}} \tag{13}$$

where Ka_Δ denotes the local Karlovitz number based on the subgrid velocity fluctuation and the filter size [35]. The model coefficient C arising in Eq. (11) can be computed assuming isotropic turbulence and has a value of $C \approx 0.07$.

It is worth noting that the present estimation was done assuming isotropic, isothermal turbulence, which is not valid in real flames. However, this hypothesis is often used for estimating subgrid quantities using resolved fields (i.e., for closure in the LES framework) and enables one to obtain reasonable results [20].

One might rewrite Eq. (12) in a closed form that is similar to the flamelet model but that is valid for describing thin reaction zones. It gives

$$\frac{\partial \bar{\rho}\,\tilde{c}}{\partial t} + \nabla(\bar{\rho}\,\tilde{\boldsymbol{u}}\,\tilde{c}) = \frac{\rho_u S_L \Xi \Delta}{b}\nabla^2\tilde{c} + \rho_u S_L \Xi \frac{1}{\Delta}\Pi_c(\tilde{c}, b) \tag{14}$$

E. Effect of Flame-Front Thickening on Flame Propagation

One considers the filtered flame propagation speed S_d, defined with respect to the unburned mixture, and introduces η, the normal coordinate across the flame front directed toward the unburned mixture. It reads

$$\rho_u S_d = \frac{\frac{\partial \bar{\rho}\,\tilde{c}}{\partial t} + \nabla(\bar{\rho}\,\tilde{\boldsymbol{u}}\,\tilde{c})}{|\nabla\tilde{c}|} = \frac{\frac{\rho_u S_L \Xi \Delta}{b}\frac{\partial^2\tilde{c}}{\partial\eta^2} + \rho_u S_L \Xi \frac{1}{\Delta}\Pi_c(\tilde{c}, b)}{|\nabla\tilde{c}|} - \kappa\frac{\rho_u S_L \Xi \Delta}{b} \tag{15}$$

where κ is the filtered flame-front curvature. It can be inferred from Eq. (15) that the thickening of the flame front also affects the propagation of the filtered flame and that the correction of the propagation speed is proportional to the curvature of the flame front. It is worth noticing that in the derivation of the G equation, Peters [27] suggested a similar expression but did not relate the curvature correction to a flame structure characteristic length.

F. Modeling of Subgrid Turbulence and Wrinkling

Equation (13) requires the estimation of the subgrid velocity fluctuation as well as the subgrid wrinkling factor. These two quantities are widely used in combustion modeling and several expressions or correlations have been proposed. Fureby [29,30] uses a transport equation to compute the SGS turbulent kinetic energy and the subgrid velocity fluctuation. Another alternative is to estimate the subgrid velocity fluctuation from the resolved velocity field. As pointed out by Colin et al. [26], the velocity fluctuation should not include thermal expansion effects. They suggest considering only the rotational part of the resolved velocity field and relate the subgrid fluctuation to the smallest resolved scales. Consequently, the subgrid velocity fluctuation u_Δ is given by

$$u_\Delta = C_2 \Delta^3 \nabla^2(\nabla \times \tilde{\boldsymbol{u}}) \tag{16}$$

where C_2 is a constant. Colin et al. [26] recommend to take $C_2 \approx 2$.

Several correlations have been proposed to relate the subgrid wrinkling to the subgrid velocity fluctuations [20,27]. Among them, Fureby [29] used the fractal concept to derive a power-law:

$$\Xi = \max\left[\left(\Gamma\frac{u_\Delta}{S_L}\right)^{D-2}, 1\right] \tag{17}$$

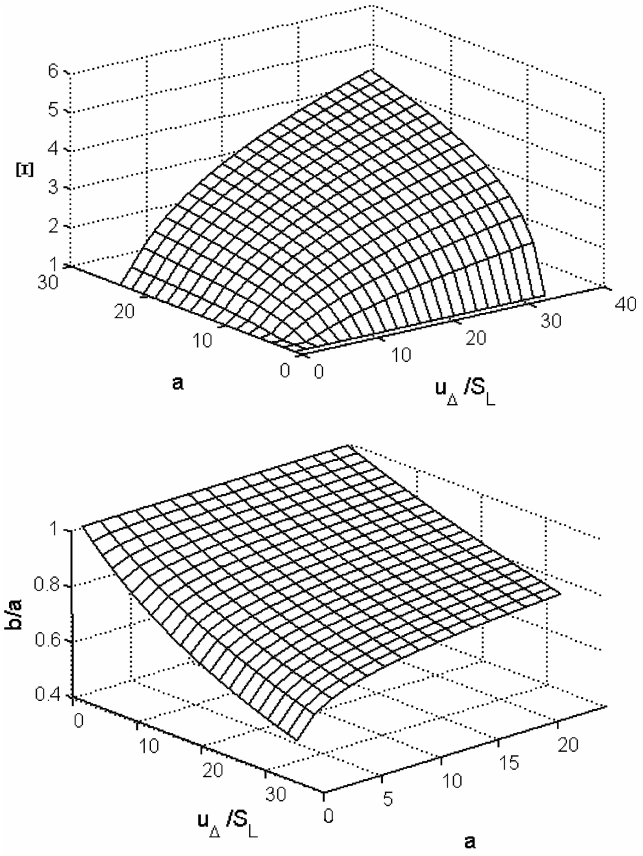

Fig. 3 Subgrid-scale wrinkling factor vs a and u_Δ/S_L (top); nondimensional ratio b/a vs a and u_Δ/S_L (bottom)

where Γ is an efficiency function presented by Meneveau and Poinsot [36]. The fractal dimension needs to be modeled and, following Fureby [30], we take

$$D = \frac{2.05}{1 + (u_\Delta/S_L)} + \frac{2.35}{1 + (S_L/u_\Delta)} \tag{18}$$

At low-velocity fluctuations, the fractal dimension tends toward 2.05 and is 2.35 when the subgrid turbulence is strong. Fureby [30] has tested the influence of different subgrid wrinkling correlations and concluded that their effect is limited on the mean flowfield predictions. He advocates the use of a relatively simple power-law [e. g., Eq. (17)].

It is worth noting that the two model constants C and C_2 arise in the closed thin-reaction-zones model. To test the sensitivity of the model to these constants, we plot the nondimensional number b and Ξ vs u_Δ/S_L and a. Figure 3 shows that the subgrid-scale wrinkling is relatively sensitive to a variation of a when it is close to one, but less when $a > 10$. In addition, at low values of a (typically, less than 10), the sensitivity of Ξ to subgrid velocity fluctuations is less than for high values of a. Because the constant C_2 enters the correlation through u_Δ/S_L, modulation of C_2 is equivalent to changing u_Δ/S_L at constant a. The model constant influences the results the most when a is high. The reason is that high values of a correspond to a filter size much larger than the flame-front thickness, and therefore the range of unresolved eddies (in the Fourier space) that wrinkle the flame front increases with a. At high values of a, Eq. (15) models a broad range of frequencies and influences the results more than at low values of a, for which the importance of the unresolved eddies is lower. Consequently, one should consider that the model constant C_2 influences the result only if a is large (typically, less than five).

Figure 3 also plots the thickening effect of the subgrid turbulence as b/a. Increasing the subgrid turbulence u_Δ/S_L will thicken the preheating zone of the flame and decrease the ratio b/a. The thickening effect is maximum at low values of a. In the upper part of the diagram, one has $b/a > 0.8$ and significant thickening effects are only seen when $a < 5$. It is worth mentioning that $a < 5$ corresponds to cases in which the subgrid turbulence is expected to be relatively week, so that u_Δ/S_L will be also relatively low (typically, less than four). Consequently, one does not expect a significant effect of thickening unless both u_Δ/S_L and a are very high.

The sensitivity of the correlation to the two constants C and C_2 can be tested by varying u_Δ/S_L while keeping a constant. One expects the thickening to be sensitive to the model constants when it is the strongest (i.e., for relatively large values of a). As pointed out by Duwig and Fuchs [31], the production term distribution Π is relatively insensitive to a for values above 10. One should conclude that the thickening effect is not expected to significantly influence the flame front and is relatively insensitive to the model constants.

G. LES Tool

The present formulation has been implemented into a finite difference implicit code that solves the semicompressible Navier–Stokes (NS) equations with variable density on Cartesian grids (density being a function of temperature only). The code is third-order accurate [23] for the convective terms and fourth-order accurate for the other terms. A second-order finite difference scheme is used for time discretization. For the progress variable, a fifth-order-weighted essentially nonoscillatory (WENO) scheme [34] is used for discretizing the convective term. The use of monotonicity preserving techniques is needed, because the c field exhibits steep gradients, typically going from zero to one over two grid cells. In addition, the resolved c field/flame front is highly wrinkled and one seeks to capture both large-scale and medium-scale wrinkling. Therefore, a high-order nonoscillatory scheme is used for the c equation.

Locally refined grids can be employed in regions with large gradients. Multigrid iterations are used to speed up the implicit NS solver. More details can be found elsewhere [37]. Using Cartesian finite differences yields easily coded, fast, and accurate results. Moreover, the implicit solver provides a stable solution strategy. These advantages make the approach most suitable for LES of reacting flows (e.g., [31]).

H. Computational Domain and Boundary Conditions

The computational domain starts 1.2 Dp upstream of the expansion and ends 12.4 Dp downstream of the expansion. The start of the computational domain corresponds to the turbulence grid location in the test rig. The inflow is modeled as a collection of small jets, corresponding to each hole of the grid. A steady Neumann inflow boundary conditions is used by imposing a steady, uniformly distributed mass flow through each hole. Incoming turbulence is difficult to model but is an important task for LES computations and remains an open question. Steady inflow conditions ensure a correct incoming mass flow but do not mimic many features of turbulence. However, the strong shear imposed at the inlet generates some turbulence. As shown in Sec. V, the level of turbulent fluctuations at the expansion is predicted correctly, in spite of no imposed turbulence in the domain.

Zero gradient outflow boundary conditions are used for all variables, together with a flux correction ensuring mass conservation. Nonslip adiabatic wall conditions (i.e., zero velocity) were enforced. Because the region of interest is relatively far from the wall boundaries, no specific measures (e.g., wall functions or grid refinements) were taken.

The computational domain includes the complete 3-D geometry. Three different computational grids have been used for evaluating the numerical accuracy. The coarser grid consists of 1,000,000 computational nodes, giving a mesh spacing of $\approx 1 \times 10^{-3}$ m in the expansion region. The medium-sized grid contained 1,500,000 nodes, with a refined region close to the expansion, and with mesh spacing of $\approx 0.6 \times 10^{-3}$ m. Finally, the finest grid contains 2,500,000 nodes. It is similar to the medium grid, but the locally refined region includes a larger part of the domain and covers the jet core down to 4 Dp after the expansion. The time step was computed using a Courant–Friedrichs–Lewy number (CFL) number ≈ 0.2 (based on the bulk velocity).

Table 1 Operating conditions investigated in the present paper[a]

Case	M	Re	Φ	P, bar	Inlet T, K	S_L, m/s	Ka	C_2	LES	OH-PLIF	PIV
1	0.12	62,500	0	1	300	——	——	——	yes	——	yes
2	0.08	15,750	0.5	1	673	0.614	3	2.0	yes	yes	——
3	0.08	31,500	0.5	2	673	0.408	4	——	——	yes	——
4	0.08	78,740	0.5	5	673	0.237	8	0.5	yes	yes	——
5	0.08	78,740	0.5	5	673	0.237	8	2.0	yes	yes	——
6	0.08	78,740	0.5	5	673	0.237	8	8.0	yes	yes	——
7	0.08	157,480	0.5	10	673	0.159	12	2.0	yes	yes	——
8	0.08	220,470	0.5	14	673	0.137	14	——	——	yes	——

$$Re = \frac{U_{\mathrm{BULK}} \cdot Dp}{\nu}, \qquad Ka = \left(\frac{u'}{S_L}\right)^{\frac{3}{2}} \cdot \left(\frac{L_{T,xx}}{\delta_L}\right)^{-\frac{1}{2}}, \qquad \delta_L = \frac{D}{S_L}$$

[a]S_L values were computed with CHEMKIN using the GRI3.0 Mechanism (http://www.me.berkeley.edu/gri_mech/). Detailed results can be found in Witt and Griebel [38]. D is the mass diffusion coefficient of methane in air; u' and $L_{T,xx}$ (based on the correlation of the axial velocity component in the x direction) were measured with PIV at the combustor inlet ($x/Dp = 0.1$, $r/Dp = 0$).

IV. Operating Conditions

Table 1 summarizes the set of operating conditions considered in the present paper. In the nonreacting case, the inflow bulk velocity was 40 m/s, giving a Reynolds number of 62,500. The operating temperature and pressure were 300 K and 101,325 Pa, respectively, giving a Mach number of 0.12.

In the reacting cases, the bulk velocity was also 40 m/s. A methane/air mixture with an equivalence ratio of $\Phi = 0.5$ was used. The fresh gas temperature was 673 K for all cases. The operating pressure was varied from 101,325 Pa to 1,418,550 Pa, keeping the Mach number constant ($M = 0.08$), corresponding to a Reynolds number varying from 15,750 up to 220,470. The Karlovitz number varies from $\approx$3 to $\approx$14. These flames fall into the so-called thin-reaction-zones regime, and the model described previously is applicable. Note that the low operating Mach number ($M = 0.08$) and the absence of strong thermoacoustic waves/instabilities [13–15] justify the use of the semicompressible (density being a function of temperature only) formulation.

The motivation for studying the effect of pressure is to verify the applicability of lower-cost atmospheric experiments to gas turbine conditions. The scaling is usually done while keeping the velocity (or Mach number) constant and decreasing the pressure and, accordingly, the Reynolds number.

For both reacting and nonreacting cases, the velocity quantities are shown dimensionless by scaling with the bulk velocity of 40 m/s, and the pipe diameter $Dp = 25 \times 10^{-3}$ m was used to scale distances.

V. Results and Discussion

A. Nonreacting Case

First, the influence of the computational grid density on the results is investigated. Figure 4 shows the normalized mean axial velocity profiles at four different axial locations in the combustor. The jet penetrates into the combustor and mass entrains, creating a recirculation zone in the outer region. All three grids capture the mean flow pattern similarly (in terms of the jet spreading rate and the recirculation zone length/strength). The coarse grid overpredicts the jet spreading slightly at $x/Dp > 5$. Figure 4 also shows the root mean square of the axial velocity fluctuation. The fluctuation levels predicted by all three grids are very similar in magnitude and in shape. The coarse grid predicts higher fluctuation for $x/Dp > 2$, resulting in a higher spreading rate, as mentioned earlier. The sensitivity of the results to the grid is low if one considers the medium and the fine grid. Consequently, the medium grid has been used for the rest of the study, which allows the reduction of the computational costs while preserving the accuracy. One should note that almost all reacting cases are characterized by a Reynolds number within the same order of magnitude and, therefore, the medium grid is suitable for simulating these cases as well.

Furthermore, predictions performed with the medium grid were compared with available PIV results. Figure 5 shows the distribution of the normalized root mean square of the axial velocity fluctuation $u_{\mathrm{RMS}}/u_{\mathrm{BULK}}$ measured with PIV, the locations of the extracted radial profiles, and the locations of the probability density functions (PDFs). Because of high-velocity gradients between the jet core and the recirculation zone, turbulence is generated in the shear layer, leading to high-velocity fluctuations in this region. The spreading of the shear layer increases with axial distance, and it finally merges at $x/Dp \approx 7$.

Radial profiles of the axial velocity are shown in Fig. 6. The LES predictions match very well with the PIV results. The jet spreading rates and the outer recirculation zone are well captured by LES. The discrepancy between the predictions of the averaged velocity fields and the experimental data is on the order of the estimated accuracy of the PIV results.

Figure 6 also shows the radial profiles of the normalized RMS of the axial velocity fluctuation. In general, the predictions agree reasonably well with the measurements. However, the comparison shows that the LES results overestimate the fluctuations in the jet core ($r/Dp < \pm 0.5$) close to the combustor inlet ($x/Dp = 0.5$) and underestimate the fluctuations in the outer zone (recirculation zone at $r/Dp > \pm 0.8$). The discrepancies in the jet core can be explained by the approximation of the inflow boundary condition and is therefore linked to the modeling of the inflow. In the recirculation zone, the computational node density was relatively low, because no gradients are expected in this region. It explains that LES captures relatively low turbulence levels in this region.

At the axial positions close to the combustor inlet and at a radius of $r/Dp = 0.5$, the RMS values are very high and the profiles show steep gradients. In the shear layer, turbulence is generated due to high-velocity gradients between the jet core and the recirculation zone, leading to high-velocity fluctuations in this region. The magnitude of these fluctuations is relatively well captured by LES.

Figure 7 shows the radial profiles of the normalized RMS of the radial velocity fluctuation. As for the axial velocity component, the LES underestimates the fluctuation in the recirculation zone. Figure 7 also shows the Reynolds stress component R_{UW} (axial/radial). The agreement is excellent between the LES and the PIV data, indicating that the present simulation well captures the turbulent momentum flux between the jet and its surroundings.

One may conclude that the overall agreement is very good, that the fluctuation levels in the shear layer are well captured, and that the discrepancy between the PIV and LES results is below the experimental uncertainty (except for that of the axial velocity fluctuations).

Figure 8 shows snapshots of the jet core taken as an isolevel of the axial velocity, as well as of the instantaneous vortex tubes. The core surface is wrinkled by the turbulent structures. In the jet, the vortices are small, corresponding to the grid turbulence, resulting in small-scale wrinkling close to the expansion. These vortical structures are responsible for the peaks seen in Figs. 6 and 7. Farther downstream,

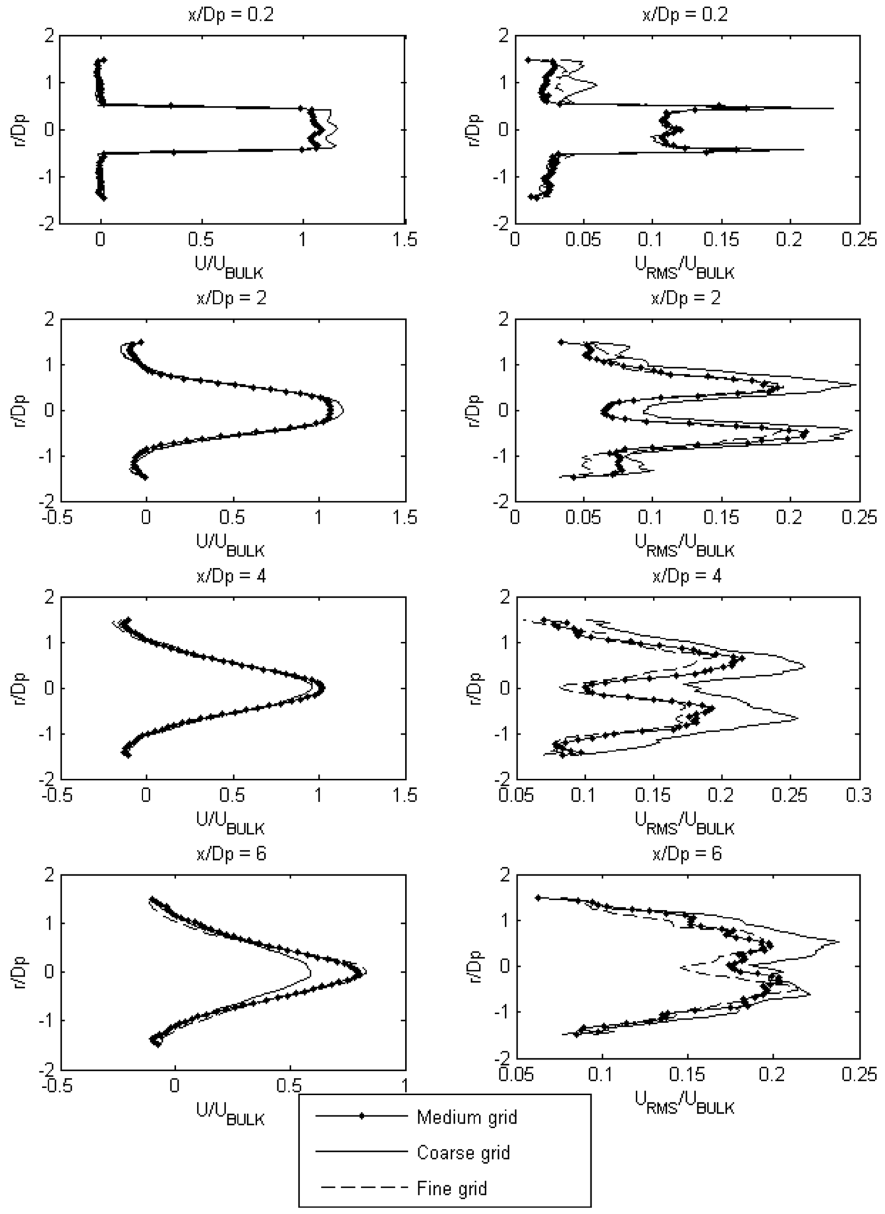

Fig. 4 Radial profiles of the normalized mean axial velocity and normalized RMS of the axial velocity fluctuation at different axial positions.

the size of the vortices and the characteristic length of the wrinkling increase. Therefore, the momentum exchange between the jet core and the surrounding fluid is amplified and results in an increase of the jet spreading rate, as seen in Fig. 6. Figure 8 also shows that the shear layer produces vortices with a nontrivial shape; the turbulence level is too high for regular vortex rings.

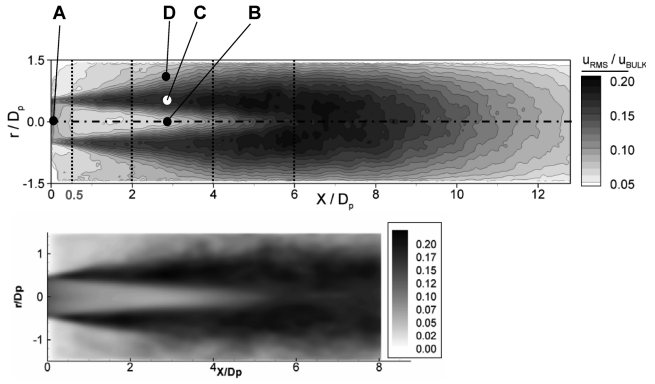

Fig. 5 Normalized root mean square of the axial velocity fluctuation $u_{\mathrm{RMS}}/u_{\mathrm{BULK}}$ measured with PIV (top) and computed by LES (bottom), together with the locations of the extracted radial profiles (Figs. 6 and 7) and of the PDFs presented in Fig. 10.

The Fourier spectra of the turbulent kinetic energy at a point located in the shear layer is shown in Fig. 9. The spectrum exhibits a high number of peaks. A typical shear-layer instability is seen (e. g., for $St \approx 0.1$, 0.13, and 0.4). It is characteristic for the turbulence generated in a jet shear layer and corresponds to the structures visualized in Fig. 8. In addition, two peaks at $St = 0.01$ and $St = 0.08$ are visible in Fig. 9. Low-frequency structures in turbulent jets were reported by Nathan et al. , corresponding to strong, but slow, precession of the jet core around the combustor axis. However, it should be emphasized that Nathan et al. considered a system with a larger expansion ratio. In the present case, the velocity fluctuations along the centerline are relatively weak compared with the levels in the shear layer, indicating that the level of turbulent kinetic energy associated with the low-frequency modes is low compared with the shear-layer-generated turbulence.

The PDF at four spatial locations (locations A to D, see Fig. 5) are presented in Fig. 10. It should be pointed out that LES very well captures the shape of the measured velocity PDF, indicating that the present computation does not only capture the averaged quantities, but also the nature and magnitude of the fluctuations.

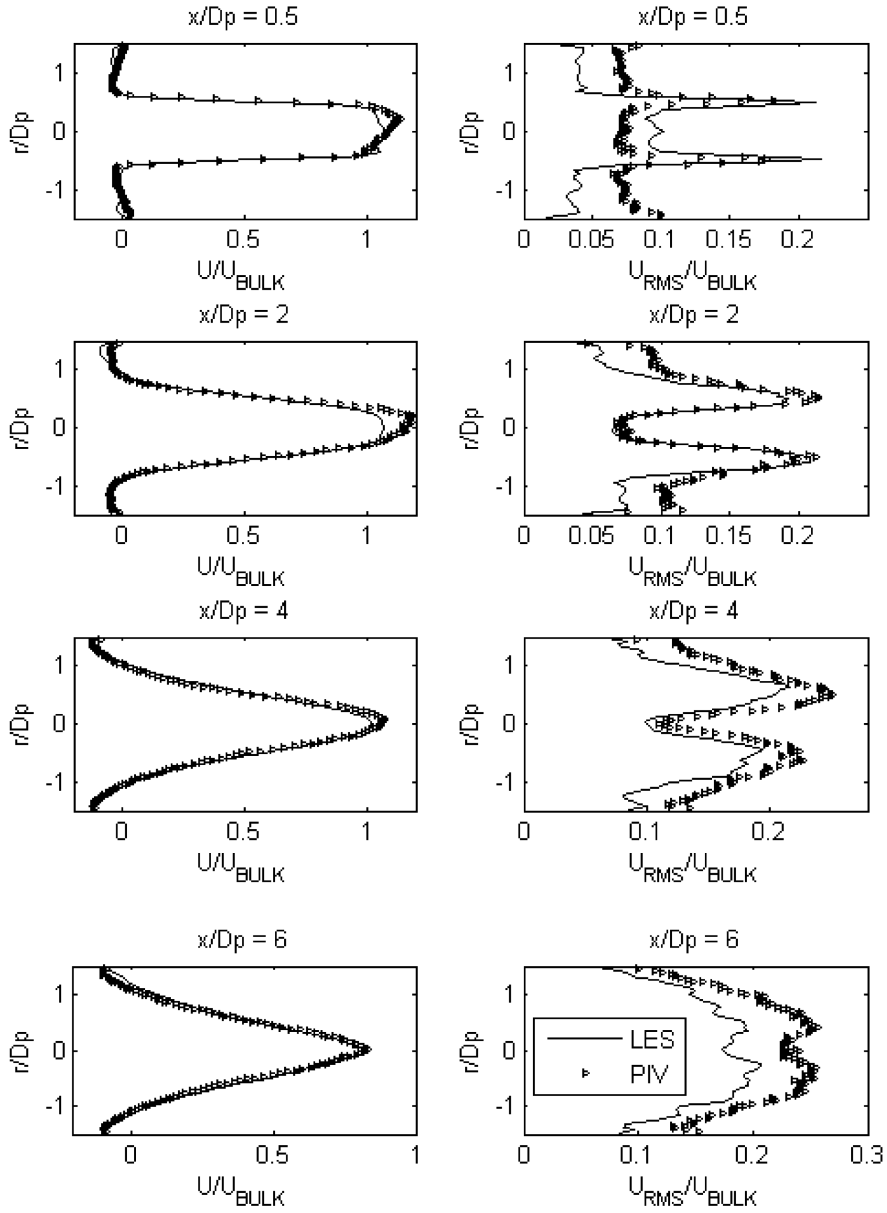

Fig. 6 Radial profiles of the normalized mean axial velocity and RMS of the axial velocity fluctuation at different axial positions.

Point A is located at the centerline in the jet core close to the expansion. The PDF has a Gaussian shape, indicating that the instantaneous velocity fluctuations are simply distributed around the mean value. In this location, one samples the grid-generated turbulence, because it is not affected by the shear layer. The velocity fluctuations are relatively strong, making the PDF curve broad. Farther downstream along the axis ($x/Dp = 3$), the width of the PDF becomes narrower, but keeps a Gaussian shape. The fluctuations at location B originate from the grid and are convected downstream without being significantly affected by the shear layer. Although convected downstream, the fluctuation decreases in intensity, because turbulence decays (explaining why the distribution is narrower). At the same axial location, one may examine the PDF at a higher radius, namely, $r/Dp = 0.5$ (in the shear layer C) and $r/Dp = 1$ (in the recirculation zone D). At both locations, the shape of the PDF is rather complex, with several peaks and a strong departure from the Gaussian distribution. The broad width of the PDF also indicates a large fluctuation amplitude of the velocity. The particular shape might suggest a slow precession of the jet core. During the precession, the shear layer will move and the location $r/Dp = 0.5$ might be in the core of the jet (relatively high velocity) or outside of the jet core (relatively low velocity).

B. Reacting Cases

1. Sensitivity to Model Constant C_2 and Comparisons of LES with PLIF

The sensitivity of the LES predictions for the reacting case at $P = 5$ bar to the model constant C_2 [see Eq. (15)] was investigated. We considered relatively strong changes in the constant value ($C_2 = 0.5$, 2, and 8). Figure 11 shows that the mean axial velocity field is not affected by the change of the model constant. Similarly, the RMS of the axial velocity field was also found to be insensitive to the change in the model constant (not shown here).

Figure 12 shows the influence of C_2 on the progress variable field. For $x/Dp < 8$, the profiles are very similar, indicating that the flame is not sensitive to the model constant. As we get closer to the tip of the flame ($x/Dp \approx 7$), the differences increase. Setting C_2 to 0.5 or 2 does not significantly change the length of the flame. However, increasing C_2 to 8 significantly changes the profile at $x/Dp = 8$. Increasing C_2 will increase the local SGS wrinkling and the local reaction rate. It will shorten the flame, as seen in Fig. 12, in which the progress variable fields obtained by OH-PLIF are also plotted. Two sets of data were considered: the time-averaged progress variable $\langle c \rangle$ and the Favre-averaged quantity $\langle \rho c \rangle / \langle \rho \rangle$. The Favre-averaged set was computed analytically from $\langle c \rangle$ using the standard formula for bimodal signals [19]. The LES data provide Favre-averaged fields.

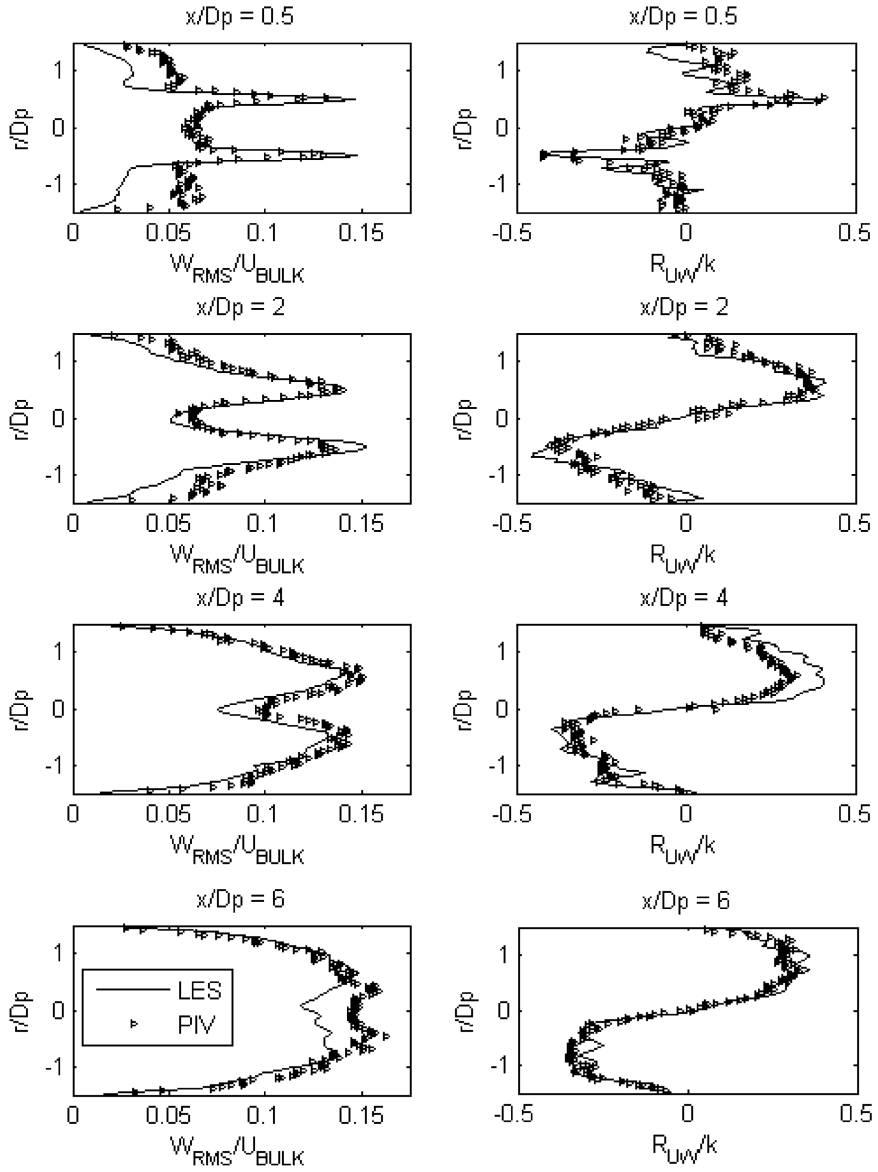

Fig. 7 Radial profiles of the normalized RMS of the radial velocity fluctuation and cross-correlation (axial-radial) R_{UW}, divided by the mean turbulent kinetic energy k, at different axial positions.

Figure 12 shows that for $x/Dp < 6$, the LES underpredicts the flame-brush thickness, which is defined as the distance between the leading edge of the flame front ($\langle c \rangle = 0.1$) and the surface for which $\langle c \rangle = 0.5$. This definition is similar to the one proposed by Karpov and Severin [40]. They defined the flame-brush thickness as the distance between the flame-front leading edge and the surface of the "half-burning" that corresponds to the progress variable $\langle c \rangle = 0.5$. Farther downstream ($6 < x/Dp < 9$), the LES predictions and PLIF results agree reasonably well for all values of C_2. This is including the flame tip location ($x/Dp > 7$), considering that both the model constant and the averaging technique (time-averaging vs Favre-averaging) significantly affect the progress variable profiles.

Finally, the LES reproduces the flame brush reasonably well, and the predictions are relatively insensitive to C_2, except at the tip of the flame. Consequently, setting C_2 to 2 is a logical choice and will be used for the rest of the study.

2. *Influence of Combustion on the Flowfield*

The reacting case at atmospheric pressure is considered first. Figure 13 (top) shows the instantaneous flame front wrinkled by vortical structures. The flame-front surface is enlarged and the turbulent flame speed is increased by turbulence. Close to the expansion, the flame-front wrinkling is due to small scales. Farther downstream, large-scale wrinkling is seen and the flame-front shape changes from quasi cylindrical to a spiral type. Figure 13 (center) also shows the vortex tubes. Vortices are generated by the grid and are convected downstream into the tube. Close to the expansion, the vortex tubes are relatively small and do not significantly modify the global flame-front pattern. Farther downstream, large-scale wrinkling occurs as large vortical structures appear. The vorticity dynamics is similar to that observed in the nonreacting case (see Fig. 7), but the large tubes appear farther downstream in the reacting case. The flame-front wrinkling can also be observed in the experimental data. Figure 13 (bottom) shows a typical OH-PLIF single-shot image.

Figure 14 shows a comparison of the axial velocity field for a reacting and a nonreacting case. At the combustor inlet, the profiles are identical. Farther downstream, the jet spreads in both cases, but in the reacting case, the spreading rate is lower. The reacting jet core is longer and wider, meaning that the reacting jet axial velocity profile longer maintains a pluglike shape. Figure 15 shows the Reynolds stress component describing the turbulent radial transport of axial momentum for both cases. It is obvious that the momentum flux is significantly lower in the reacting case for $x/Dp < 7$. The momentum transport from the jet to the recirculation zone is

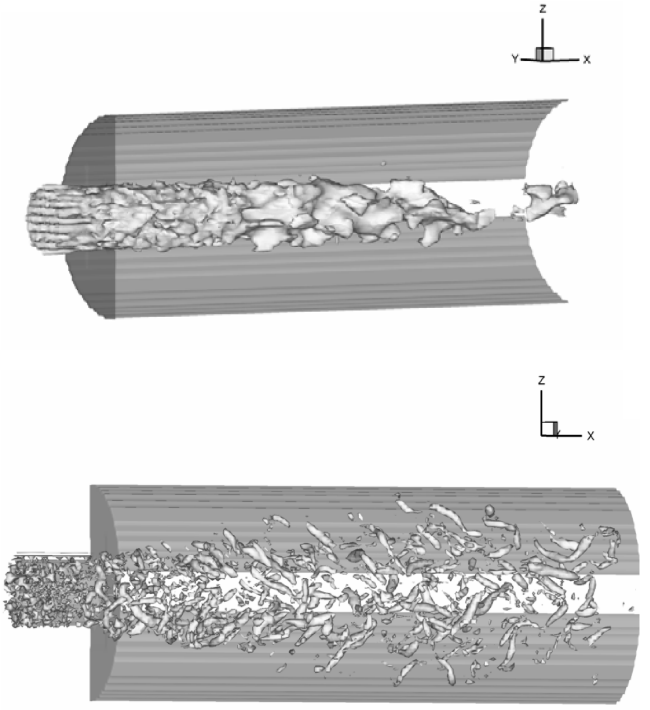

Fig. 8 Snapshot of the axial velocity level $U/U_{\mathrm{BULK}} = 0.75$ (top); snapshot of the vorticity tubes visualized as isolevels of λ_2 [41] (bottom).

therefore lower in the reacting case, explaining why the nonreacting jet spreads faster than the reacting case. This phenomenon is known as countergradient transport (CGT) (e.g., [9]). It describes the effect of a thermal expansion within a shear layer. The differential acceleration of the cold gases (the jet) and the hot combustion products (recirculation zone) lowers the gradient across the shear layer and, consequently, across the entrainment of the jet. In this particular setup, CGT slightly decreases the axial expansion of the jet core and the outer recirculation strength. A similar behavior has also been observed in free jets [9].

Figure 16 (left) shows the axial velocity PDF in the shear layer at an axial distance of 3 Dp from the expansion (location D in Fig. 5). The shape of the PDF is not Gaussian and several peaks are visible. Comparing this PDF with the corresponding one in Fig. 10 indicates a similar shape, but a narrower distribution. In particular, the positive velocity side in Fig. 16 is truncated. This is expected, because the

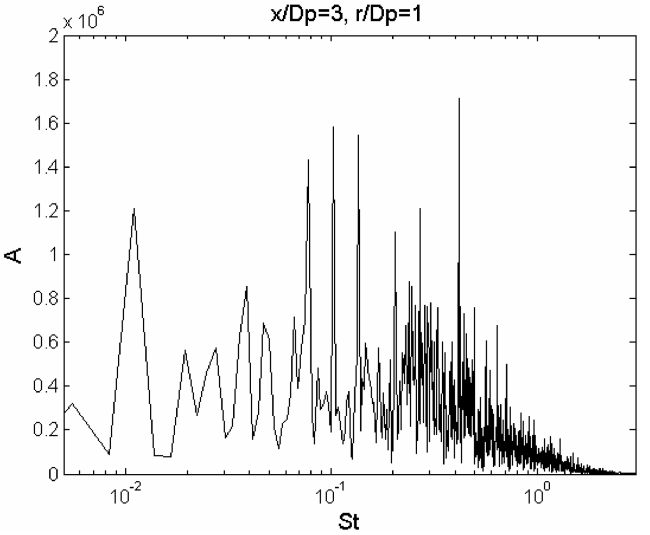

Fig. 9 Power spectra of the turbulent kinetic energy vs Strouhal number ($St = f \cdot Dp/U_{\mathrm{BULK}}$) at point D.

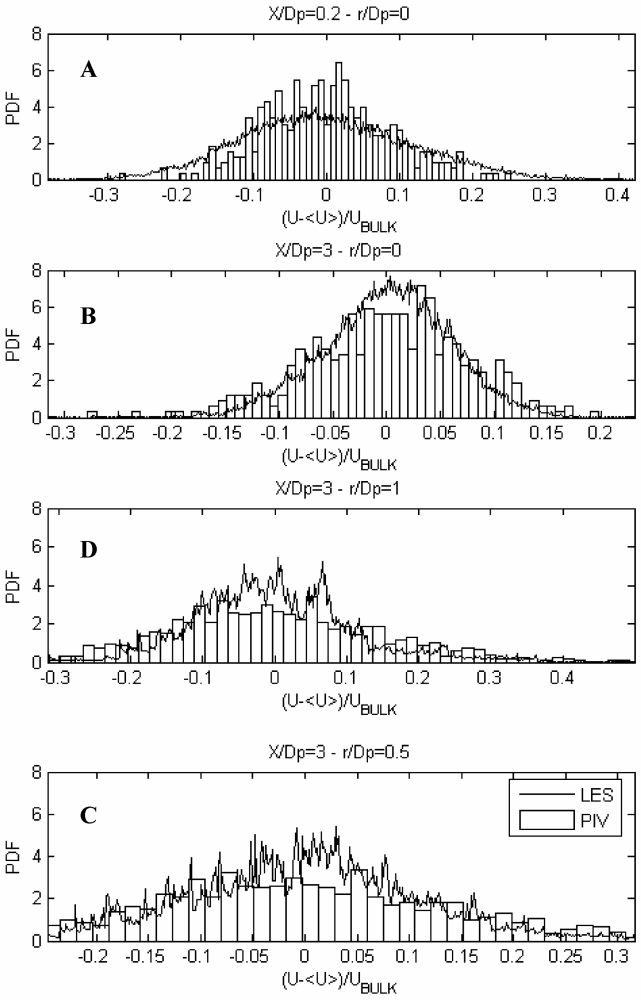

Fig. 10 PDFs of the reduced axial velocity at four different locations.

axial momentum transfer toward higher radius is lower in the reacting case. Figure 16 (right) shows the frequency spectra. As for the nonreacting case, both high- and low-frequency peaks are observed. However, the frequency range is shifted toward lower frequencies. For instance, the shear-layer instabilities are seen at $St \sim 0.1$, whereas in the cold case, it was around $St \sim 0.4$. This shift in the frequency range can be explained by thermal expansion, because the sampling point is located in the burned gases. Lower-frequency peaks are also seen with $St \sim 0.001$. The present spectrum has been obtained over more than 100,000 time iterations, and it has not been possible to significantly extend the sampling time for capturing peaks around the very low frequency of $St \sim 0.001$. The results suggest that the thermal expansion modifies the frequency of the characteristic modes, but does not suppress them.

3. *Influence of Pressure on the Flowfield*

The experimental and numerical study was also conducted by varying the operating pressure between 1 and 14 bar and keeping the Mach number, the equivalence ratio, and the fresh gas temperature constant, thereby varying the Reynolds and Karlovitz numbers (see Table 1). Figures 17 and 18 show the Favre-averaged progress variable fields obtained using OH-PLIF and LES. The OH-PLIF results document that pressure does not significantly influence the progress variable field. The strongest discrepancy between the LES and the PLIF results is seen at $x/Dp < 7$ at relatively low pressures ($P < 2$ bar). Part of this discrepancy can be attributed to reflections, which were particularly a problem at these low-pressure conditions because of the extremely high OH signal intensities. This also explains the shape of the radial c profiles at 1 bar (relative maximum at $r/Dp \approx \pm 0.8$). The LES results also indicate that the c profile is

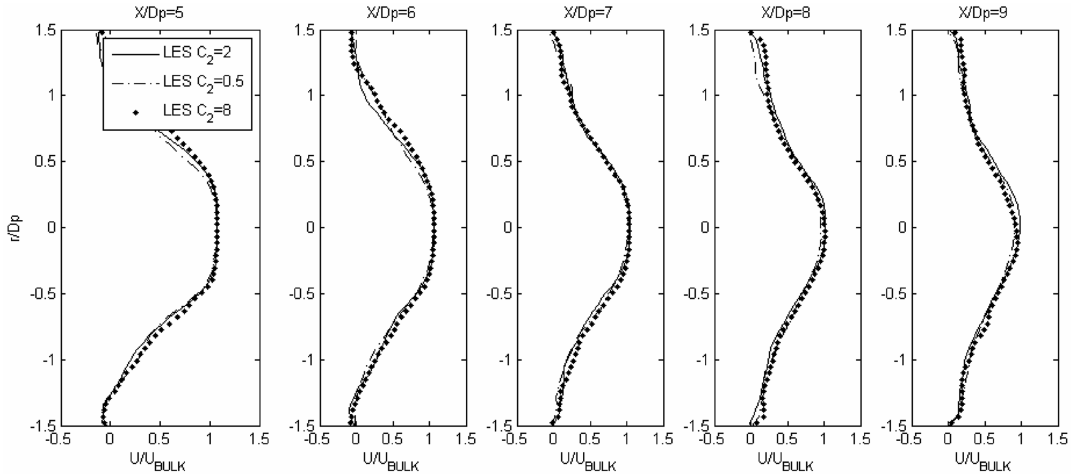

Fig. 11 Radial profiles of the normalized mean axial velocity at different axial positions predicted by LES for different values of the model constant C_2. The operating pressure was 5 bar.

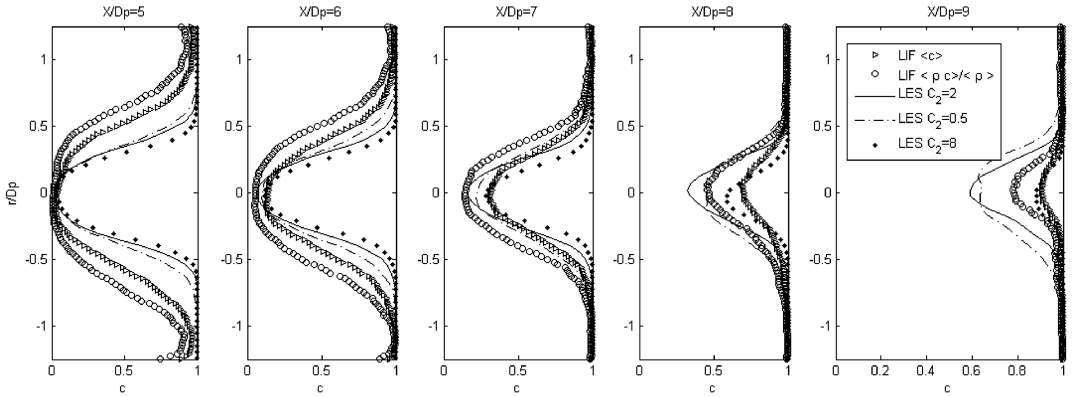

Fig. 12 Radial profiles of the progress variable at different axial positions. The operating pressure was 5 bar.

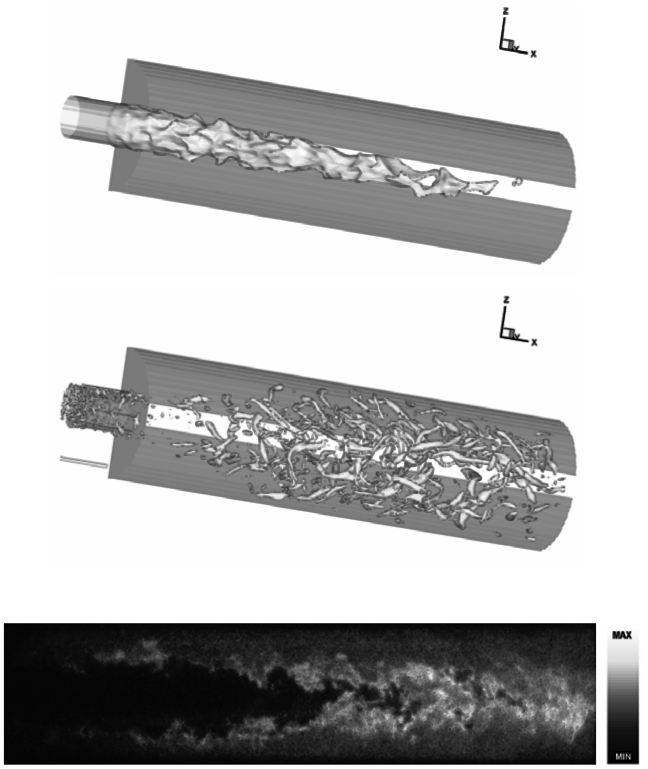

Fig. 13 Snapshot of the flame front, isosurface $c = 0.5$ (top); snapshot of the vorticity tubes visualized as isolevels of λ_2 [41] (center); and typical OH-PLIF single shot, 5 bar, $\Phi = 0.50$ (bottom).

not sensitive to the operating pressure. A slight departure from the three curves is seen at $x/Dp = 7.9$, but one should notice that the difference is smaller than that observed previously (e.g., sensitivity to C_2). Figure 19 shows the mean and RMS of the axial velocity obtained by LES for the different operating pressures. The axial velocity profile or its fluctuations are not sensitive to the operating pressure (i.e., to the Reynolds or Karlovitz numbers) in the range considered. One should also notice that the flow pattern and the flame stabilization mechanism (i.e., recirculation of hot gases) are not affected by changing the Reynolds number. However, the Karlovitz number changes dramatically with pressure without affecting the mean progress variable field.

Figure 20 (top) shows the PDF of the nondimensional parameter b, which accounts for the thickening of the flame front [see Eq. (12)]. At $P = 1$ bar, b does not fluctuate strongly and the PDF shows a well-defined peak at $b \approx 6$. We are close to the flamelet regime, and the broadening effects due to turbulence entering the preheating zone are low. Increasing the pressure or Karlovitz number implies that the preheating zone of the flame front will be increasingly affected by turbulence. Consequently, the PDF of b broadens with increasing pressure, as seen in Fig. 20. Increasing the operating pressure from 1 to 5 bar (changing the pressure by a factor of 5) modifies the PDF of b significantly and doubles the value of b (from $\approx$6 to $\approx$12). A further increase of pressure from 5 to 10 bar (factor 2) only slightly changes b. For pressures above 5 bar, the variation of b is only weakly dependent on pressure. Consequently, it will not have a strong influence on the production rate Π shape. Figure 20 (bottom) shows the PDF of the nondimensional flame SGS propagation speed $(S_L[-]/U_o)$ at different operating pressures. One notices that at $P = 1$ bar, the PDF exhibits a strong peak close to $\sim$0.013, corresponding to the limit $[-] = 1$. The subgrid turbulence is

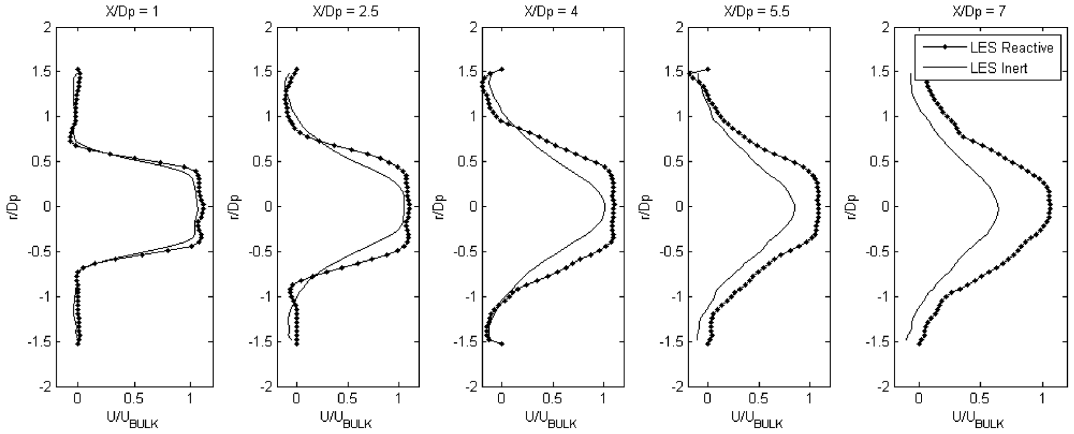

Fig. 14 Radial profiles of the normalized mean axial velocity at different axial positions from LES predictions with and without reaction. The operating pressure was 1 bar.

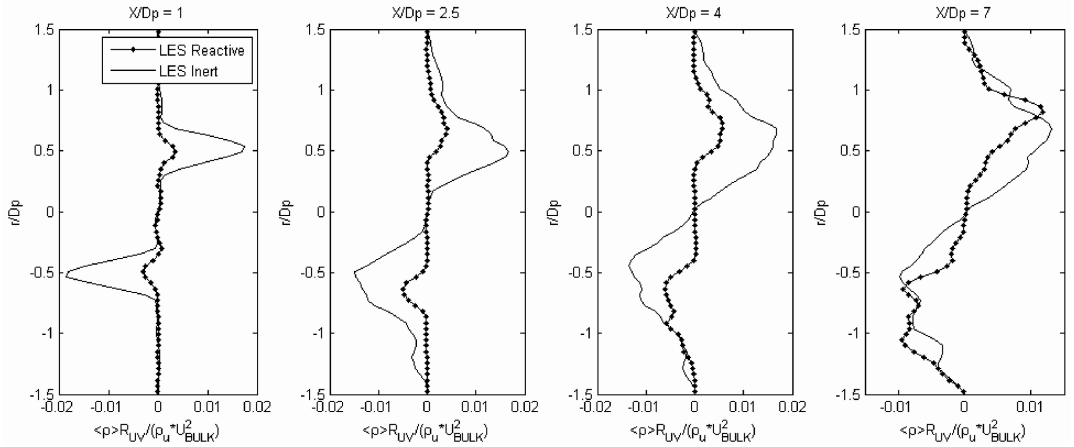

Fig. 15 Radial profiles of the normalized Reynolds stress tensor component R_{UV} at different axial positions from LES predictions with and without reaction. The operating pressure was 1 bar.

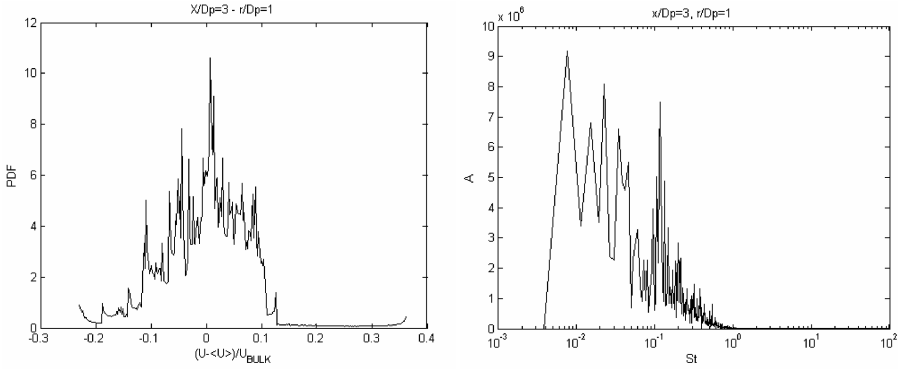

Fig. 16 Axial velocity PDF at point D (left); turbulent kinetic energy frequency spectra at point D vs Strouhal number (right).

relatively weak in this particular case, and the predicted subgrid wrinkling is low (typically, below two) and has a small effect on the flame. Changing the pressure from 1 to 10 bar does not significantly change the absolute values of the SGS propagation speed and the PDF. This can be explained by the fact that the dramatic decrease of S_L with pressure ($S_L \sim P^{-0.5}$) is compensated by an increase of the subgrid wrinkling ([-]). Consequently, no term of Eq. (13) will exhibit a dramatic change with pressure.

Although turbulence strongly affects the flame-front structure by increasing the flame-front wrinkling and by broadening the flame preheating zone, the net effect on the mean quantities such as progress variable and axial velocity was found to be small.

VI. Conclusions

A detailed investigation of a turbulent confined jet and jet flame has been presented in this paper. Numerical simulations and laser measurements of nonreacting and reacting conditions were performed. The reacting conditions correspond to a lean premixed flame relevant for gas turbine applications. Large eddy simulation

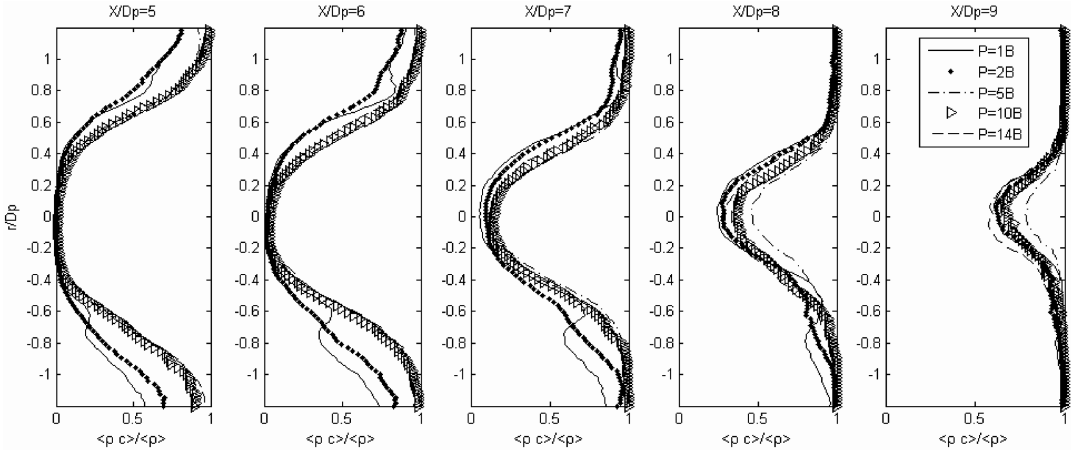

Fig. 17 Radial profiles of the Favre-averaged progress variable at different axial positions extracted from OH-PLIF measurements at different operating pressures.

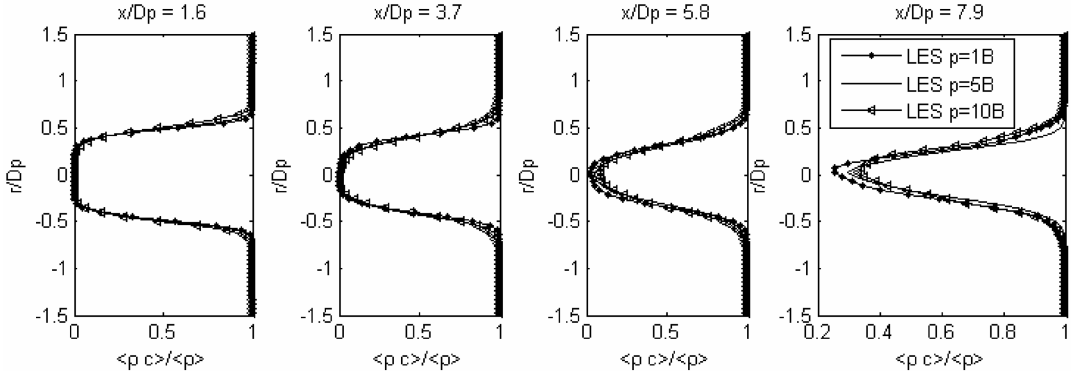

Fig. 18 Radial profiles of the Favre-averaged progress variable at different axial positions predicted by LES for different operating pressures.

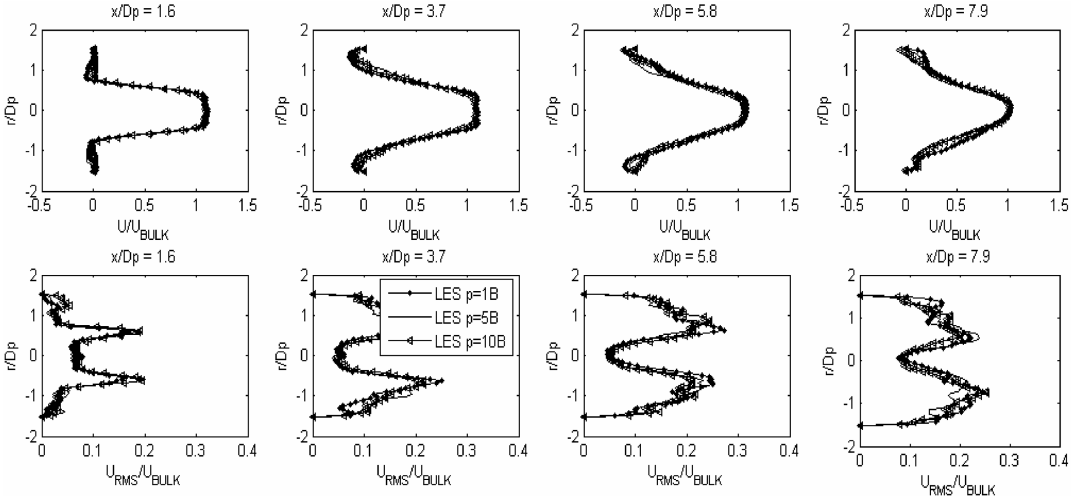

Fig. 19 Radial profiles of the normalized axial velocity (averaged and RMS) at different axial positions predicted by LES for different operating pressures.

was used to investigate the flowfield and was supplemented with a LES flamelet model for capturing the flame dynamics. The velocity field of the nonreacting case was averaged and compared with experimental PIV results. The agreement was excellent for both the mean and the RMS values. The numerical simulation suggested that the jet core exhibits a slow and weak precession.

The simulations of the reacting cases showed that the thermal expansion across the flame front lowers the momentum exchange between the jet core and the recirculation zone. Consequently, the jet core was found to be slightly longer and broader in the reacting case. One may argue that the preheating of the fuel/air mixture reduces the density jump across the flame front and, consequently, lowers its effect on the flowfield. In addition, LES and OH-PLIF data showed that the operating pressure has no significant influence on the velocity field or on the averaged progress variable field. It was also shown that the decrease of laminar flame speed with pressure was compensated by an increase of flame-front wrinkling. The net result of the pressure influence was found to be insignificant. These findings support the relevance of isothermal or atmospheric experiments/simulations for understanding the flow/flame dynamics

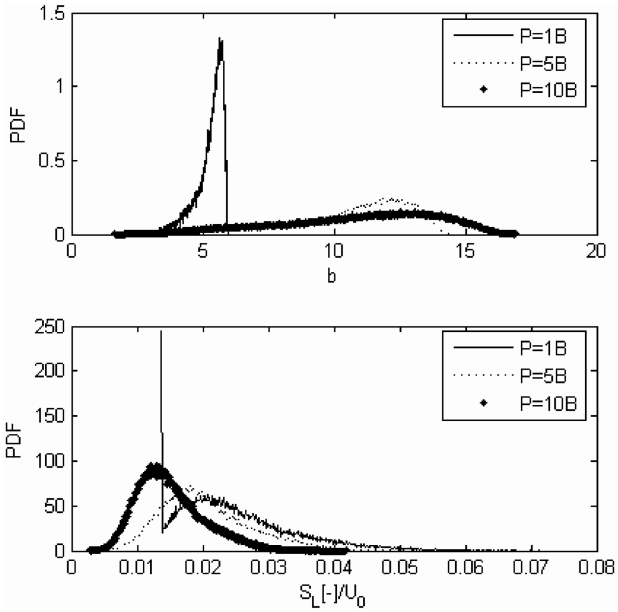

Fig. 20 Probability function of *b* and the normalized SGS flame speed at one randomly chosen time step for different operating pressures.

in nonswirling jet combustors. They also show the possibility of extending this understanding to reacting cases at higher pressure.

Acknowledgments

This work was partially supported by the Swedish Energy Authority (STEM) and by the Swedish Research Council (VR). The experimental portion of this work was financially supported by the Swiss Federal Office of Energy (BFE), which is gratefully acknowledged. The authors of this portion would also like to thank Daniel Erne for the technical support and Rolf Bombach, Andreas Inauen, and Sabine Schenker from the Paul Scherrer Institut (PSI) Combustion Diagnostics Group for their help in setting up and operating the laser system, as well as for the stimulating discussions about laser spectroscopy. The computations were run on LUNAC and HPC2N facilities within the allocation program SNAC. The authors want to thank Luis Urbina for performing some early simulations.

References

[1] Lefebvre, A. H., "The Role of Fuel-Preparation in Low-Emission Combustion," *Journal of Engineering for Gas Turbines and Power*, Vol. 117, No. 44, 1995, pp. 617–654.

[2] Olsson, M., and Fuchs, L., "Large Eddy Simulation of a Force Semi-Confined Circular Impinging Jet," *Physics of Fluids*, Vol. 10, No. 2, 1998, pp. 476–486.

[3] Olsson, M., and Fuchs, L., "Large Eddy Simulation of the Proximal Region of a Spatially Developing Circular Jet," *Physics of Fluids*, Vol. 8, No. 8, 1996, pp. 2125–2135.

[4] Grinstein, F. F., Gutmark, E. J., Parr, T. P., Hanson-Parr, D. M., and Obeysekare, U., "Streamwise and Spanwise Vortex Interaction in an Axi-Symmetric Jet: A Computational and Experimental Study," *Physics of Fluids*, Vol. 8, No. 6, 1996, pp. 1515–1524.

[5] Grinstein, F. F., "Vortex Dynamics and Entrainment in Regular Free Jets," *Journal of Fluid Mechanics*, Vol. 437, 2001, pp. 69–101.

[6] Dasilva, C., and Métais, O., "Vortex Control of Bifurcating Jets: A Numerical Study," *Physics of Fluids*, Vol. 14, No. 2, 2002, pp. 3798–3819.

[7] Dellenback, P. A., Metzger, D. E., and Neitzel, G. P., "Measurements in Turbulent Swirling Flow Through an Abrupt Axisymmetric Expansion," *AIAA Journal*, Vol. 26, No. 6, 1988, pp. 669–681.

[8] Kobayashi, H., Nakashima, T., Tamura, T., Maruta, K., and Niioka, T., "Turbulence Measurements and Observations of Turbulent Premixed Flames at Elevated Pressures up to 3.0 mPa," *Combustion and Flame*, Vol. 108, Nos. 1–2, 1997, pp. 104–117.

[9] Chen Y-C., Peters, N., Schneemann, G. A., Wruck, N., Renz, U., and Mansour, M. S., "The Detailed Flame Structure of Highly Turbulent Premixed Methane-Air Flames," *Combustion and Flame*, Vol. 107, No. 3, 1996, pp. 233–244.

[10] Buschmann, A., Dinkelacker, F., Schäfer, T., Schäfer, M., and Wolfrum, J., "Measurement of the Instantaneous Detailed Flame Structure in Turbulent Premixed Combustion," *Proceedings of the Combustion Institute*, Vol. 26, Combustion Inst., Pittsburgh, PA, 1996, pp. 437–445.

[11] Kobayashi, H., Tamura, T., Maruta, K., and Niioka, T., "Burning Velocity of Turbulent Premixed Flames in a High-Pressure Environment," *Proceedings of the Combustion Institute*, Vol. 26, Combustion Inst., Pittsburgh, PA, 1996, pp. 389–396.

[12] Lachaux, T., Halter, F., Chauveau, C., Gokalp, I., and Shepherd, I. G., "Flame Front Analysis of High-Pressure Turbulent Lean Premixed Methane-Air Flames," *Proceedings of the Combustion Institute*, Vol. 30, Combustion Inst., Pittsburgh, PA, 2005, pp. 819–826.

[13] Griebel, P., Schären, R., Siewert, P., Bombach, R., Inauen, A., and Kreutner, W., "Flowfield and Structure of Turbulent High-Pressure Premixed Methane/Air Flames," American Society of Mechanical Engineers Paper GT2003-38398, 2003.

[14] Griebel, P., Schären, R., Siewert, P., Bombach, R., Inauen, A., and Kreutner, W., "Flame Characteristics and Turbulent Flame Speeds of Turbulent, High-Pressure, Lean Premixed Methane/Air Flames," American Society of Mechanical Engineers Paper GT2005-68565, 2005.

[15] Griebel, P., Siewert, P., and Jansohn, P., "Flame Characteristics of Turbulent Lean Premixed Methane/Air Flames at High Pressure," *Proceedings of the Combustion Institute* (to be published).

[16] Siewert, P., "Flame Front Characteristics of Turbulent Lean Premixed Methane/Air Flames at High Pressure," Ph.D. Thesis No. 16369, Swiss Federal Inst. of Technology, Zurich, Switzerland, Feb. 2006; also available at http://e-collection.ethbib.ethz.ch/cgi-bin/show.pl?type=-diss&nr=16369&lang=en.

[17] Durst, F., Melling, A., and Whitelaw, J. H., *Principles and Practice of Laser-Doppler Anemometry*, Academic Press, New York, 1981.

[18] Anon., "DaVis FlowMaster Software Manual for DaVis 6.2," LaVision, Göttingen, Germany, 2002.

[19] Deschamps, B. M., Smallwood, G. J., Prieur, J., Snelling, D. R., and Gülder, Ö. L., "Surface Density Measurements of Turbulent Premixed Flames in a Spark-Ignition Engine and a Bunsen-Type Burner Using Planar Laser-Induced Fluorescence," *Proceedings of the Combustion Institute*, Vol. 26, Combustion Inst., Pittsburgh, PA, 1996, pp. 427–435.

[20] Poinsot, T., and Veynante, D., *Theoretical and Numerical Combustion*, R. T. Edwards, Philadelphia, 2001.

[21] Fureby, C., and Grinstein, F. F., "Large Eddy Simulation of High-Reynolds Number Free- and Wall-Bounded Flows," *Journal of Computational Physics*, Vol. 181, No. 1, 2002, pp. 68–97.

[22] Grinstein, F. F., and Fureby, C., "Recent Progress On Miles for High Reynolds Number Flows," *Journal of Fluids Engineering*, Vol. 124, No. 4, 2002, pp. 848–861.

[23] Rai, M. M., and Moin, P., "Direct Simulations of Turbulent Flow Using Finite Difference Schemes," *Journal of Computational Physics*, Vol. 96, No. 1, 1991, pp. 15–53.

[24] Revstedt, J., Gullbrand, J., Guillard, F., Fuchs, L., and Trägårdh, C., "Large Eddy Simulation of Mixing in an Impinging Jet," *Proceedings of the 4th ECOMAS Computational Fluid Dynamics Conference*, Wiley, New York, 1998, pp. 1169–1174.

[25] Grinstein, F. F., and Kailasanath K. K, "Three Dimensional Numerical Simulations of Unsteady Reactive Square Jets," *Combustion and Flame*, Vol. 100, 1994, pp. 2–10.

[26] Colin, O., Ducros, F., Veynante, D., and Poinsot, T., "A Thickened Flame Model for Large Eddy Simulation of Turbulent Premixed Combustion," *Physics of Fluids*, Vol. 12, No. 7, 2000, pp. 1843–1863.

[27] Peters, N., *Turbulent Combustion*, Cambridge Univ. Press, New York, 2001.

[28] Weller, H. G., Tabor, G., Gosman, A. D., and Fureby, C., "Application of a Flame-Wrinkling Les Combustion Model To a Turbulent Shear Layer Formed at a Rearward Facing Step," *Proceedings of the Combustion Institute*, Vol. 27, Combustion Inst., Pittsburgh, PA, 1998, pp. 899–907.

[29] Fureby, C., "A Fractal Flame-Wrinkling Large Eddy Simulation Model for Premixed Turbulent Combustion," *Proceedings of the Combustion Institute*, Vol. 30, Combustion Inst., Pittsburgh, PA, 2005, pp. 593–601.

[30] Fureby, C., "A Comparison of Flamelet Les Models for Premixed Turbulent Combustion," Proceedings of the 44th AIAA Aerospace Sciences Meeting and Exhibit, Reno, NV, AIAA Paper 2006-155, 2006.

[31] Duwig, C., and Fuchs, L., "Study of Flame Stabilization in a Swirling

Combustor Using a New Flamelet Formulation," *Combustion Science and Technology*, Vol. 177, Aug. 2005, pp. 1485–1510.

[32] Domingo, P., Vervisch, L., Payet, S., and Hauguel, R., "DNS of a Premixed Turbulent V Flame and LES of a Ducted Flame Using a FSD-PDF Subgrid Scale Closure with FPI-Tabulated Chemistry," *Combustion and Flame*, Vol. 143, No. 4, 2005, pp. 566–586.

[33] Chakravarthy, V., and Menon, S., "Large-Eddy Simulation of Turbulent Premixed Flames in the Flamelet Regime," *Combustion Science and Technology*, Vol. 162, Jan. 2001, pp. 1–50.

[34] Jiang, G-S., and Shu, C-W., "Efficient Implementation of Weighted ENO Schemes," *Journal of Computational Physics*, Vol. 126, No. 1, 1996, pp. 202–228.

[35] Pitsch, H., and Duchamps, L., "Large Eddy Simulation of Premixed Turbulent Combustion Using a Level Set Approach," *Proceedings of the Combustion Institute*, Vol. 29, Combustion Inst., Pittsburgh, PA, 2002, pp. 2001–2008.

[36] Meneveau, C., and Poinsot, T., "Stretching and Quenching of Flamelets in Premixed Turbulent Combustion," *Combustion and Flame*, Vol. 86, No. 4, 1991, pp. 311–332.

[37] Gullbrand, J., Bai, X. S., and Fuchs, L., "High-Order Cartesian Grid Method for Calculation of Incompressible Turbulent Flows," *International Journal for Numerical Methods in Fluids*, Vol. 36, No. 6, 2001, pp. 687–709.

[38] Witt, M., and Griebel, P., "Numerische Untersuchung von laminaren Methan/Luft-Vormischflammen," Paul Scherrer Inst., Rept. TM-50-00-07, 2000, pp. 1–26.

[39] Nathan, G. J., Hill, S. J., and Luxton, R. E., "An Axisymmetric 'Fluidic' Nozzle to Generate Jet Precession," *Journal of Fluid Mechanics*, Vol. 370, pp. 347–380.

[40] Karpov, V. P., and Severin, E. S., "Turbulent Burn-Up Rates of Propane-Air Flames Determined in a Bomb with Agitators," *Combustion, Explosion, and Shock Waves*, Vol. 14, No. 2, 1978, pp. 158–163.

[41] Joeng, J., and Hussain, F., "On the Identification of a Vortex," *Journal of Fluid Mechanics*, Vol. 285, 1995, pp. 69–94.

C. Kaplan
Associate Editor